

## Estimating the black hole spin for the X-ray binary MAXI J1820+070

Xueshan Zhao,<sup>1,2</sup> Lijun Gou,<sup>1,2</sup> Yanting Dong,<sup>1,3</sup> Youli Tuo,<sup>2,4</sup> Zhenxuan Liao,<sup>1,2</sup> Yufeng Li,<sup>1,2</sup> Nan Jia,<sup>1,2</sup> Ye Feng,<sup>1,2</sup> and James F. Steiner<sup>5</sup>

<sup>1</sup>*Key Laboratory for Computational Astrophysics, National Astronomical Observatories, Chinese Academy of Sciences, Datun Road A20, Beijing 100012, China*

<sup>2</sup>*School of Astronomy and Space Sciences, University of Chinese Academy of Sciences, Datun Road A20, Beijing 100049, China*

<sup>3</sup>*Zhejiang Institute of Modern Physics, Department of Physics, Zhejiang University, 38 Zheda Road, Hangzhou 310027, China*

<sup>4</sup>*Key Laboratory of Particle Astrophysics, Institute of High Energy Physics, Chinese Academy of Sciences, 19B Yuquan Road, Beijing 100049, People's Republic of China*

<sup>5</sup>*Harvard-Smithsonian Center for Astrophysics, Cambridge, MA 02138, United States*

### ABSTRACT

MAXI J1820+070 is a newly-discovered black hole X-ray binary, whose dynamical parameters, namely the black hole mass, the inclination angle and the source distance, have been estimated recently. *Insight*-HXMT have observed its entire outburst from 2018 March 14. In this manuscript, we fitted the spectra obtained by *Insight*-HXMT in the soft state to a fully-relativistic thin disk model KERRBB2, and found a slowly-spin black hole of  $a_* = 0.13_{-0.10}^{+0.07}$  ( $1\sigma$ ) with the continuum-fitting method.

*Keywords:* *Insight*-HXMT, black hole physics, X-rays:binaries, X-rays: individual (MAXI J1820+070)

### INTRODUCTION

The spin is a crucial parameter of a black hole, which is helpful to understand the driving mechanism of the relativistic jets (Blandford & Znajek 1977), to explore the fundamental physic around the black hole (Wong et al. 2012), to test the predictions of general relativity (Bambi & Barausse 2011, Bambi & Modesto 2013, Tripathi et al. 2020). We usually use a dimensionless parameter  $a_*$  to represent the spin, defining  $a_* \equiv a/M = cJ/GM^2$ , where  $M$  and  $J$  represent the black hole mass and the angular momentum. In the traditional electromagnetic (EM) domain, we can only estimate the spin with some indirect techniques since the spin only makes itself notable via the general relativistic (GR) effect within a small region around the event horizon<sup>1</sup>. So far, there have developed two widely-used methods to measure the spin parameter of accreting stellar-mass black holes: (1) the continuum-fitting method, which models the shape of the thermal emission from the accretion disk (Zhang et al. 1997); (2) the reflection-fitting method, which models the red wing of the relativistically-broadened and asymmetric Fe K $\alpha$  line (Fabian et al. 1989, Reynolds & Nowak 2003).

The key process of the spin measurements is to estimate the radius of the inner disk  $r_{\text{in}}$  ( $r_{\text{in}} \equiv R_{\text{in}}/M$  in standard general relativistic units).  $R_{\text{in}}$  is assumed to be equal to the radius of the innermost stable circular orbit  $R_{\text{ISCO}}$  (Shafee et al. 2008, Reynolds & Fabian 2008, Penna et al. 2010, Kulkarni et al. 2011, Noble et al. 2009, Noble et al. 2010, Noble et al. 2011), which is a monotonic function of the dimensionless spin parameter  $a_*$ , decreasing from  $6 GM/c^2$  to  $1 GM/c^2$  as the spin increases from  $a_* = 0$  to  $a_* = 1$  (Bardeen et al. 1972).

MAXI J1820+070 is a newly-discovered transient source. Its optical counterpart, ASASSN-18ey, was discovered by the All-Sky Automated Survey for SuperNovae (ASAS-SN, Shappee et al. 2014) on 2018 March 6 at R.A. =  $18^{\text{h}}20^{\text{m}}21.^{\text{s}}9$  dec. =  $+07^{\circ}11'07.''3$  (J2000) (Tucker et al. 2018). In X-ray, it was found by the Monitor of All-sky X-ray Image (MAXI, Matsuoka et al. 2009) on March 11, 2018 (Kawamuro et al. 2018). Since discovery, the X-ray outburst of MAXI J1820+070 displayed a fast increase, and then a slow decay (MJD 58200-MJD 58290) in flux. The source

Corresponding author: Xueshan Zhao, Lijun Gou  
xszhao@nao.cas.cn, lgou@nao.cas.cn

<sup>1</sup> It is noted that both the gravitational wave (Abbott et al. 2020) and Event Horizon Telescope (EHT) observations can directly constrain the black hole spin. The gravitational wave observations have provided spin constraints for tens of merging black hole systems, however, as to EHT, although it can resolve the event horizons for certain black holes, due to its limited resolution, it is hard to give a direct spin constraint currently (Event Horizon Telescope Collaboration et al. 2019).

underwent its first re-brightening (MJD 58290-MJD 58305) and then dropped sharply as transiting to the soft state. The source stayed in the soft state for over 2 months (till around MJD 58380) before its second re-brightening due to transiting back to the hard state. After around MJD 58400, the source faded away into quiescence. During the entire eruption, this source showed all of the accretion state (Remillard & McClintock 2006): the thermal dominant state (TD), or the high/soft state (HSS); the low/hard state (LHS); the steep power law (SPL) state (the so-called intermediate state in some literature). In order to ensure the reasonable application of the continuum-fitting method, we focus on spectra dominated by thermal accretion disk component avoiding the interference introduced by the strong Comptonization component.

In the continuum-fitting method, one determines  $r_{\text{in}}$  by fitting the X-ray thermal continuum from the accretion disk to the Novikov-Thorne thin disk model (Novikov & Thorne 1973). Given that the disk luminosity  $L \propto 2\pi D^2 F(\cos i)^{-1} \propto 4\pi R_{\text{ISCO}}^2 T_{\text{eff}}^4$  (where  $F$ ,  $T_{\text{eff}}$ ,  $D$ ,  $i$  indicate the X-ray flux, the effective temperature, the distance to the source and the inclination angle), we have  $r_{\text{ISCO}}^2 \propto F/(2 T_{\text{eff}}^4) (\cos i)^{-1} D^2 (M^{-2})$ . Therefore three dynamical parameters, namely the black hole mass  $M$ , the disk inclination  $i$  and the source distance  $D$ , are crucial for estimating the spin. There have been systematic measurements to determine these three parameters. Torres et al. (2019) reported a mass function  $f(M) \equiv (M_1 \sin i)^3 / (M_1 + M_2)^2 = 5.18 \pm 0.15 M_{\odot}$  (where  $M_1$  and  $M_2$  indicate the masses of the black hole and the donor star), dynamically confirming a black hole harboring in this binary. Assuming a provisional mass ration  $q \equiv M_2/M_1 = 0.12$ , they constrained the binary inclination to be  $69^\circ \lesssim i \lesssim 77^\circ$  and derived a black hole mass in the range of 7-8  $M_{\odot}$ . Atri et al. (2020) calculated the distance to be  $D = 2.96 \pm 0.33$  kpc via the measurement of the radio parallax using the Very Long Baseline Array (VLBA) and the European Very Long Baseline Interferometry (VLBI) Network. Further they used the distance and estimated the jet inclination angle and the black hole mass to be  $63 \pm 3^\circ$  and  $9.2 \pm 1.3 M_{\odot}$  (adopting  $q = 0.12$ ), respectively. A few months later, Torres et al. (2020) analyzed intermediate resolution optical spectroscopy, leading to a direct and accurate determination of  $q = 0.072 \pm 0.012$ . Their constraints to the binary inclination  $66^\circ < i < 81^\circ$  based on the detection of eclipse and measurements of the accretion disk radius at the time of the optical spectroscopy, ignoring the disk vertical structure. The revised black hole mass is  $5.96 M_{\odot} < M < 8.06 M_{\odot}$ . They also reported that adopting  $63 \pm 3^\circ$  (Atri et al. 2020) leads to  $M = 8.48_{-0.72}^{+0.79} M_{\odot}$ , with uncertainties quoted at  $1\sigma$ . We adopt  $M = 8.48_{-0.72}^{+0.79} M_{\odot}$ ,  $i = 63 \pm 3^\circ$  and  $D = 2.96 \pm 0.33$  kpc, which in turn are used as input parameters to constrain the spin of MAXI J1820+070 via the continuum-fitting method.

Many previous work have studied the characteristics of MAXI J1820+070, especially, the behaviour of inner disk radius (which implies the spin) of the black hole. Kara et al. (2019) performed spectra and temporal analysis on MAXI J1820+070, suggesting that during the outburst, the corona reduced in the spatial extent, while the inner disk didn't truncate ( $< 2R_g$ ). Bharali et al. (2019) fitted spectra obtained by *Swift* and *NuSTAR* in the hard state, constrained the inner disk radius and the disc inclination angle to be  $5.1_{-0.7}^{+1.0} R_g$  and  $29.8_{-2.7}^{+3.0}^\circ$  ( $3\sigma$ ). By investigating the spectra evolution of the entire outburst using data from *MAXI* and *Swift*, Shidatsu et al. (2019) showed that the state transition occurred at its first re-brightening phase, suggesting that it is not determined by the mass accretion rate alone. They gave the constraint of the inner disk to be  $R_{\text{in}} = 77.9 \pm 1.0 (D/3 \text{ kpc}) (\cos i / \cos 60^\circ)^{-1/2}$  km during the high/soft state. Buisson et al. (2019) analyzed data obtained by *NuSTAR* during the hard state, reporting a small stable inner radius, which implies a low to moderate spin black hole. Fabian et al. (2020) discovered an excess emission between 6-10 keV during the soft state observed by *NuSTAR* and *NICER*, which can be well-modelled by an additional BBODY. They explained this excess to be the emission from the edge of the plunge region where matter begins to fall into the black hole. Both Fabian et al. (2020) and Buisson et al. (2019) reported that if the inner disk inclination lies between  $30\text{-}40^\circ$ , then the spin lies in the range of  $\pm 0.5$ . However, there has been no specific work to measure the spin of the black hole in MAXI J1820+070. Therefore, in this paper, we attempt to estimate the spin of this source by the continuum-fitting method.

This paper is organized as follows. In Section 2, we describe our observations and data reduction. In Section 3, we report our spectral analysis and fit results. Discussion and conclusion are showed in Section 4.

## OBSERVATIONS AND DATA REDUCTION

The *Hard X-ray Modulation Telescope* (HXMT, also named *Insight*)<sup>2</sup> was successfully launched on June 15th, 2017. There are three main detectors onboard *Insight*-HXMT<sup>3</sup>: the low energy X-ray telescope (LE, 1-15 keV, SCD, 384

<sup>2</sup> <http://www.hxmt.org>

<sup>3</sup> <http://www.hxmt.org/index.php/enhome/enabouthxmt/160-hard-x-ray-modulation-telescope>

cm<sup>2</sup>); the medium energy X-ray telescope (ME, 5-30 keV, Si-Pin, 952 cm<sup>2</sup>); the high energy X-ray telescope (HE, 20-250 keV, NaI(Tl)/CsI(Na), 5100 cm<sup>2</sup>) (Liu et al. 2020, Zhang et al. 2020, Chen et al. 2020, Cao et al. 2020). It began fixed-point observations for MAXI J1820+070 on 2018 March 14 (MJD 58191), and monitored the whole outburst of this source until 2018 October 21 (MJD 58412).

Spectra were extracted using *Insight*-HXMT Data Analysis Software (HXMTDAS) v2.02 following a standard procedure. Only spectra from events that belong to the small FoV (1.6° × 6° for LE and 1° × 4° for ME) were extracted. We simply used observations from LE and ME detectors, given that these instruments have already provided adequate energy coverage. The spectra were rebinned using GRPHA with at least 100 counts per new bin (Kaastra & Bleeker 2016). We also added systematic errors due to uncertainties of the instrumental responses: 1% for LE and 2% for ME (Chen et al. 2020, Cao et al. 2020). Spectral analyzed was performed on XSPEC v12.10.1. In this work, we utilized 2-10 keV for LE and 10-25 keV for ME.

## SPECTRAL ANALYSIS

### *Non-Relativistic Models*

Figure 1 displays HXMT observations of MAXI J1820+070 during the 2018 outburst. As an empirical choice, we ignored spectra with hardness larger than 0.5, since our targets are the spectra dominated by thermal emission.

We first applied a preliminary non-relativistic model on these spectra, which is expressed as CONSTANT\*TBABS\*SIMPL\*DISKBB (hereafter, NR). The equivalent hydrogen column density in TBABS was fixed to  $0.15 \times 10^{22} \text{ cm}^{-2}$  to account for the Galactic absorption (Uttley et al. 2018). In the empirical Comptonization model SIMPL, the parameter  $f_{\text{sc}}$  calculates the fraction of the thermal seed photons that are scattered into the power-law tail (Steiner et al. 2009b). Steiner et al. (2009a) suggested that the inner disk radius (i.e. the spin) remains stable to within a few percent as  $f_{\text{sc}} \lesssim 25\%$ . Thereafter it became a widely-utilized spectral selection criteria in the continuum-fitting measurements of the spin. Because SIMPL redistributes seed photons to both lower and higher energies where the response matrices of HXMT are limited, we extended the sampled energies to 0.1-100 keV on XSPEC (see the appendix of Steiner et al. 2009b). In the non-relativistic multicolors black body model DISKBB, two crucial parameters are estimated, namely the temperature ( $T_{\text{in}}$ ) and the radius ( $R_{\text{in}}$ ) of the inner accretion disk.

Fitting results to NR model are listed in Table 2. For NR, It can be seen obviously that the  $f_{\text{sc}}$  of these spectra all satisfy  $f_{\text{sc}} \lesssim 25\%$ , with the central values ranging from 0.015 to 0.167. The temperature at inner disk radius  $T_{\text{in}}$  shows a small decline, lying in a range of 0.749-0.488 keV with the average value of 0.680 keV. The normalization of DISKBB is defined as  $(R_{\text{in}}/D_{10})^2 \cos i$ . Adopting  $M = 8.48^{+0.79}_{-0.72} M_{\odot}$ ,  $i = 63 \pm 3^{\circ}$  and  $D = 2.96 \pm 0.33$  kpc, we calculated the inner edge of the disk  $R_{\text{in}}$  in the unit of  $R_{\text{g}}$  (the gravitational radius  $R_{\text{g}} \equiv GM/c^2 = 12.55$  km for  $M = 8.48 M_{\odot}$ ). The best-fitting value of  $R_{\text{in}}$  varies slightly from  $4.41R_{\text{g}}$  to  $5.20R_{\text{g}}$ . The average of  $R_{\text{in}}$  is  $4.69R_{\text{g}}$ . The value of  $R_{\text{in}}$  estimated from DISKBB implies a small spin parameter. However, we were unable to constrain the photon index  $\Gamma$  of SP25-52, probably owing to the weak Comptonization component and the lower counts rate in  $E > 10$  keV.

### *Relativistic Models*

Next, we substituted DISKBB (Mitsuda et al. 1984, Makishima et al. 1986) with KERRBB2 (McClintock et al. 2006). The reconstructed model is expressed as CONSTANT\*TBABS\*SIMPL\*KERRBB2 (hereafter, RM). KERRBB2 is a fully-relativistic thin disk model and is the combination of BHSPEC (Davis et al. 2005) and KERRBB (Li et al. 2005). This model reads in a pair of look-up tables for the spectral hardening factor  $f$  ( $f \equiv T_{\text{col}}/T_{\text{eff}}$ ) estimated by BHSPEC corresponding to two typical values of the viscosity parameter  $\alpha$ : 0.1 and 0.01.  $a_*$  decreases slightly as  $\alpha$  increases, so that throughout this work, we adopt  $\alpha = 0.01$  in order to make a more conservative limitation. Fit results for  $\alpha = 0.1$  are listed in Table 4.  $\alpha = 0.01$  gives larger values of  $a_*$  that  $\alpha = 0.1$ , with  $\Delta a_*$  varying from 0.041 to 0.070. We have also fitted spectra for  $\alpha = 0.1$ . Specifically, referring to Shidatsu et al. (2019), the parameter  $\Gamma$  of SP25-52 is fixed to 2.5, a representative value for the soft state. We tested different  $\Gamma$ , and fit results are presented in Table 6. It is showed that  $a_*$  decreases by  $\Delta a_* = 0.024$  as  $\Gamma$  increases from 2.00 to 2.80. For other spectra, we allowed  $\Gamma$  to vary.

The best-fit results are showed in Table 3. In RM, the  $f_{\text{sc}}$  of SP61 is  $26.2\% \pm 0.3\%$ , slight above 25%. And the values of  $f_{\text{sc}}$  in SP55-61 ( $24.4\% \pm 0.3\%$ ,  $23.8\% \pm 0.2\%$ ,  $24.2\% \pm 0.3\%$ ,  $13.6\% \pm 0.2\%$ ,  $13.0\% \pm 0.3\%$ ,  $26.2\% \pm 0.3\%$ ) are significantly larger than that of other 54 spectra. It means that the strength of the Comptonization component in SP1-54 is faint, contributing less than 10% of the total emission. The spin measurement using the continuum-fitting method based on those 54 spectra will be more robust. In fact, in SP55-61, MAXI J1820+070 underwent the state transition. Shidatsu et al. (2019) divided these 7 spectra into the intermediate state (IM).

Therefore, we treated these spectra as our “gold” spectra, mainly basing our analysis and error analysis on them although almost all the spectra meet the selection criteria  $f_{\text{sc}} \lesssim 25\%$ . Meanwhile, SP55-61 (hereafter, “silver” spectra) were also analyzed just as reference. In Table 2 and Table 3, we used horizontal lines to distinguish the “gold” spectra.

For all the “gold” spectra, our model provides a good fit, with the reduced  $\chi^2_{\nu}$  varying between 0.84-1.17. A representative plot of the unfolded spectrum is given in Figure 2. The best-fit value of  $a_*$  lies in the range from 0.034 to 0.213, with the mean of 0.128, confirming a slowly-spin black hole in MAXI J1820+070.

### Error Analysis

The errors quoted in Table 2 and Table 3 are only due to the statistic uncertainties estimated via XSPEC. The confidence level is 90%. As mentioned in Section 1, the error budget of  $a_*$  is dominated by the combined observational uncertainties of  $M$ ,  $i$  and  $D$ . Herein the Monte Carlo (MC) simulation was performed for error analysis. The steps of error analysis are described as following: for each individual spectrum, (1) assuming independent and Gaussian distributed, we generate 3000 sets of  $(M, i, D)$ . (2) we calculate look-up tables of  $f$  for these parameter sets. (3) we re-fit the spectrum 3000 times with these  $(M, i, D)$  to determine the histograms of  $a_*$ , from which we finally decide the error of  $a_*$ .

We made MC simulations on 54 “gold” spectra. Histograms of  $a_*$  are plotted in Figure 3, and the summed histogram is showed in Figure 4. Adopting the histogram, we arrived at the final value of  $a_* = 0.13^{+0.07}_{-0.10}$  ( $1\sigma$ ).

## DISCUSSION AND CONCLUSION

Shidatsu et al. (2019) estimated the inner edge of the accretion disk in the HSS to be  $R_{\text{in}} = 77.9 \pm 1.0 (D/3 \text{ kpc})(\cos i / \cos 60^\circ)^{-1/2}$  km. Using  $M = 8.48^{+0.79}_{-0.72} M_{\odot}$ ,  $i = 63 \pm 3^\circ$  and  $D = 2.96 \pm 0.33$  kpc, the black hole in MAXI J1820+070 is near non-rotating. We constrained the spin to be  $a_* = 0.13^{+0.07}_{-0.10}$  ( $1\sigma$ ), which is basically compatible with their work.

Torres et al. (2020) gave the black hole mass as a function of the binary inclination  $M = \frac{5.95 \pm 0.22}{\sin^3 i} M_{\odot}$ . They made a limitation on  $i$  on the basis of binary geometrical arguments:  $i < 80.8^\circ$  as the absence of X-ray eclipses during the outburst;  $i > 66.2^\circ$  as the condition that during the outburst the disk reached the 3:2 resonance radius. Adopting this constraints, they reported a mass range of  $5.96 M_{\odot} < M < 8.06 M_{\odot}$  ( $1\sigma$ ). On the other hand, the jet inclination angle was refined as  $i = 63 \pm 3^\circ$  from the measured proper motions of the jet in radio band (Atri et al. 2020), which results in  $M = 8.48^{+0.79}_{-0.72} M_{\odot}$  at  $1\sigma$ .<sup>4</sup> Referring to Figure 5, the spin parameter decreases as the mass decreases or the inclination increases. Given that the spin of this source is slow, we can give a more conservative estimation adopting a larger  $M$  together with a smaller  $i$ . That is, in our work, we regarded the jet inclination angle  $i = 63 \pm 3^\circ$  as the disk inclination, and utilized corresponding  $M = 8.48^{+0.79}_{-0.72} M_{\odot}$  as the black hole mass. We have also used  $i = 66.2^\circ$  and  $M = 8.06 M_{\odot}$  to constrain the upper limit of the spin for Torres’s parameters. The fitting results are shown in Table 5. The best-fit values of the spin are below zero, so that Torres’s parameter configuration may leads to a retrograde black hole, which needs to be checked with the precise system parameters in the future. Furtherly, assuming  $M = 8.06 M_{\odot}$ , the spin will peg to its lower limit -0.99 in KERRBB2 if the inclination is above  $70^\circ$ . The critical value of  $i$  is  $67^\circ$  for  $M = 5.96 M_{\odot}$ .

In addition, it is noted that the reflection spectral fit to the *NuSTAR* prefers a smaller inner disk inclination between 30%-40% (Bharali et al. 2019, Buisson et al. 2019, Fabian et al. 2020). The spin derived from the soft-state *NuSTAR* spectra is almost maximally retrograde ( $a_* < -0.95$ , Fabian et al. 2020) if the disk inclination is about  $70^\circ$ .

As a caveat, all the spin measurements from the continuum-fitting method (Liu et al. 2008, Gou et al. 2009, Gou et al. 2010, Steiner et al. 2011, Steiner et al. 2012, Gou et al. 2014, Steiner et al. 2014, Chen et al. 2016, Steiner et al. 2016) basically suggested positive spin values, and there has been no clear observational evidence for the existence of retrograde black holes. Morningstar et al. (2014) initially reported a retrograde spin for the black hole in Nova Muscae 1991:  $a_* = -0.25^{+0.05}_{-0.64}$  (90% confidence level). However, Chen et al. (2016) found a moderately high value of spin,  $a_* = 0.63^{+0.16}_{-0.19}$  ( $1\sigma$  confidence level) after the system parameters were updated consistently, and rule strongly against a retrograde value:  $a_* > 0.17$  ( $2\sigma$  or 95.4% confidence level). Mainly because the spin of the black hole depends on the measurement of the disk inclination, the black hole mass and the distance to the source. For the MAXI J1820+070 discussed here, we only provided a conservative estimation of the spin using the continuum-fitting method, more accurate dynamical parameters are required for detailed spin measurements in the future.

<sup>4</sup> Torres et al. (2020) noted that if there exists an opening angle  $\lesssim 20^\circ$  (constrained observationally in neutron star low-mass X-ray binaries, Jiménez-Ibarra et al. 2018), the lower limit to  $i$  will decrease to be compatible with the jet orientation angle.

In this work, we report *Insight*-HXMT spectral measurements of the spin parameter  $a_*$  to the newly-observed black hole X-ray binary MAXI J1820+070. Using the continuum-fitting method, adopting  $M = 8.48_{-0.72}^{+0.79} M_\odot$ ,  $i = 63 \pm 3^\circ$  and  $D = 2.96 \pm 0.33$  kpc, we deduce a conservative value of  $a_* = 0.13_{-0.10}^{+0.07}$  ( $1\sigma$ ), showing that the black hole in this system is rotating slowly. Besides, applying  $5.96 M_\odot < M < 8.06 M_\odot$  and  $66^\circ < i < 81^\circ$  instead leads to a retrograde spin black hole.

## ACKNOWLEDGMENTS

This work made use of the data from the *Insight*-HXMT mission, a project funded by China National Space Administration (CNSA) and the Chinese Academy of Sciences (CAS). The authors thank supports from the National Program on Key Research and Development Project (Grant No. 2016YFA0400800 and 2016YFA0400801) and from the NSFC (U1838201 and U1838202). L.J.G. acknowledges the support by the National Program on Key Research and Development Project (Grant No. 2016YFA0400804), and by the NSFC (U1838114), and by the Strategic Priority Research Program of the Chinese Academy of Sciences (XDB23040100).

## REFERENCES

- Abbott, R., Abbott, T. D., Abraham, S., & et al. 2020, arXiv e-prints, arXiv:2010.14527.  
<https://arxiv.org/abs/2010.14527>
- Atri, P., Miller-Jones, J. C. A., Bahramian, A., et al. 2020, MNRAS, 493, L81, doi: [10.1093/mnras/laaa010](https://doi.org/10.1093/mnras/laaa010)
- Bambi, C., & Barausse, E. 2011, ApJ, 731, 121, doi: [10.1088/0004-637X/731/2/121](https://doi.org/10.1088/0004-637X/731/2/121)
- Bambi, C., & Modesto, L. 2013, Physics Letters B, 721, 329, doi: <https://doi.org/10.1016/j.physletb.2013.03.025>
- Bardeen, J. M., Press, W. H., & Teukolsky, S. A. 1972, ApJ, 178, 347, doi: [10.1086/151796](https://doi.org/10.1086/151796)
- Bharali, P., Chauhan, J., & Boruah, K. 2019, MNRAS, 487, 5946, doi: [10.1093/mnras/stz1686](https://doi.org/10.1093/mnras/stz1686)
- Blandford, R. D., & Znajek, R. L. 1977, MNRAS, 179, 433, doi: [10.1093/mnras/179.3.433](https://doi.org/10.1093/mnras/179.3.433)
- Buisson, D. J. K., Fabian, A. C., Barret, D., et al. 2019, MNRAS, 490, 1350, doi: [10.1093/mnras/stz2681](https://doi.org/10.1093/mnras/stz2681)
- Cao, X. L., Jiang, W. C., Meng, B., et al. 2020, Sci. China-Phys. Mech. Astron, 63(4): 249504.  
<https://arxiv.org/abs/1910.04451>
- Chen, Y., Cui, W. W., Li, W., et al. 2020, Sci. China-Phys. Mech. Astron, 63(4): 249505, doi: [10.1007/s11433-019-1469-5](https://doi.org/10.1007/s11433-019-1469-5)
- Chen, Z. H., Gou, L. J., McClintock, J. E., et al. 2016, ApJ, 825, 45, doi: [10.3847/0004-637X/825/1/45](https://doi.org/10.3847/0004-637X/825/1/45)
- Davis, S. W., Blaes, O. M., Hubeny, I., & Turner, N. J. 2005, ApJ, 621, 372, doi: [10.1086/427278](https://doi.org/10.1086/427278)
- Event Horizon Telescope Collaboration, Akiyama, K., Alberdi, A., et al. 2019, ApJL, 875, L1, doi: [10.3847/2041-8213/ab0ec7](https://doi.org/10.3847/2041-8213/ab0ec7)
- Fabian, A. C., Rees, M. J., Stella, L., & White, N. E. 1989, MNRAS, 238, 729, doi: [10.1093/mnras/238.3.729](https://doi.org/10.1093/mnras/238.3.729)
- Fabian, A. C., Buisson, D. J., Kosec, P., et al. 2020, MNRAS, 493, 5389, doi: [10.1093/mnras/staa564](https://doi.org/10.1093/mnras/staa564)
- Gou, L., McClintock, J. E., Steiner, J. F., et al. 2010, The Astrophysical Journal, 718, L122, doi: [10.1088/2041-8205/718/2/L122](https://doi.org/10.1088/2041-8205/718/2/L122)
- Gou, L. J., McClintock, J. E., Liu, J. F., et al. 2009, ApJ, 701, 1076, doi: [10.1088/0004-637X/701/2/1076](https://doi.org/10.1088/0004-637X/701/2/1076)
- Gou, L. J., McClintock, J. E., Remillard, R. A., et al. 2014, ApJ, 790, 29, doi: [10.1088/0004-637X/790/1/29](https://doi.org/10.1088/0004-637X/790/1/29)
- Jiménez-Ibarra, F., Muñoz-Darias, T., Wang, L., et al. 2018, MNRAS, 474, 4717, doi: [10.1093/mnras/stx2926](https://doi.org/10.1093/mnras/stx2926)
- Kaasra, J. S., & Bleeker, J. A. M. 2016, A&A, 587, A151, doi: [10.1051/0004-6361/201527395](https://doi.org/10.1051/0004-6361/201527395)
- Kara, E., Steiner, J. F., Fabian, A. C., et al. 2019, Nature, 565, 198, doi: [10.1038/s41586-018-0803-x](https://doi.org/10.1038/s41586-018-0803-x)
- Kawamuro, T., Negoro, H., Yoneyama, T., et al. 2018, The Astronomer's Telegram, 11399, 1
- Kulkarni, A. K., Penna, R. F., Shcherbakov, R. V., et al. 2011, MNRAS, 414, 1183, doi: [10.1111/j.1365-2966.2011.18446.x](https://doi.org/10.1111/j.1365-2966.2011.18446.x)
- Li, L. X., Zimmerman, E. R., Narayan, R., & McClintock, J. E. 2005, ApJS, 157, 335, doi: [10.1086/428089](https://doi.org/10.1086/428089)
- Liu, C. Z., Zhang, Y. F., Li, X. F., et al. 2020, Sci. China-Phys. Mech. Astron, 63(4): 249503.  
<https://arxiv.org/abs/1910.04955>
- Liu, J. F., McClintock, J. E., Narayan, R., Davis, S. W., & Orosz, J. A. 2008, ApJ, 679, L37, doi: [10.1086/588840](https://doi.org/10.1086/588840)
- Makishima, K., Maejima, Y., Mitsuda, K., et al. 1986, ApJ, 308, 635, doi: [10.1086/164534](https://doi.org/10.1086/164534)
- Matsuoka, M., Kawasaki, K., Ueno, S., et al. 2009, PASJ, 61, 999, doi: [10.1093/pasj/61.5.999](https://doi.org/10.1093/pasj/61.5.999)
- McClintock, J. E., Shafee, R., Narayan, R., et al. 2006, ApJ, 652, 518, doi: [10.1086/508457](https://doi.org/10.1086/508457)

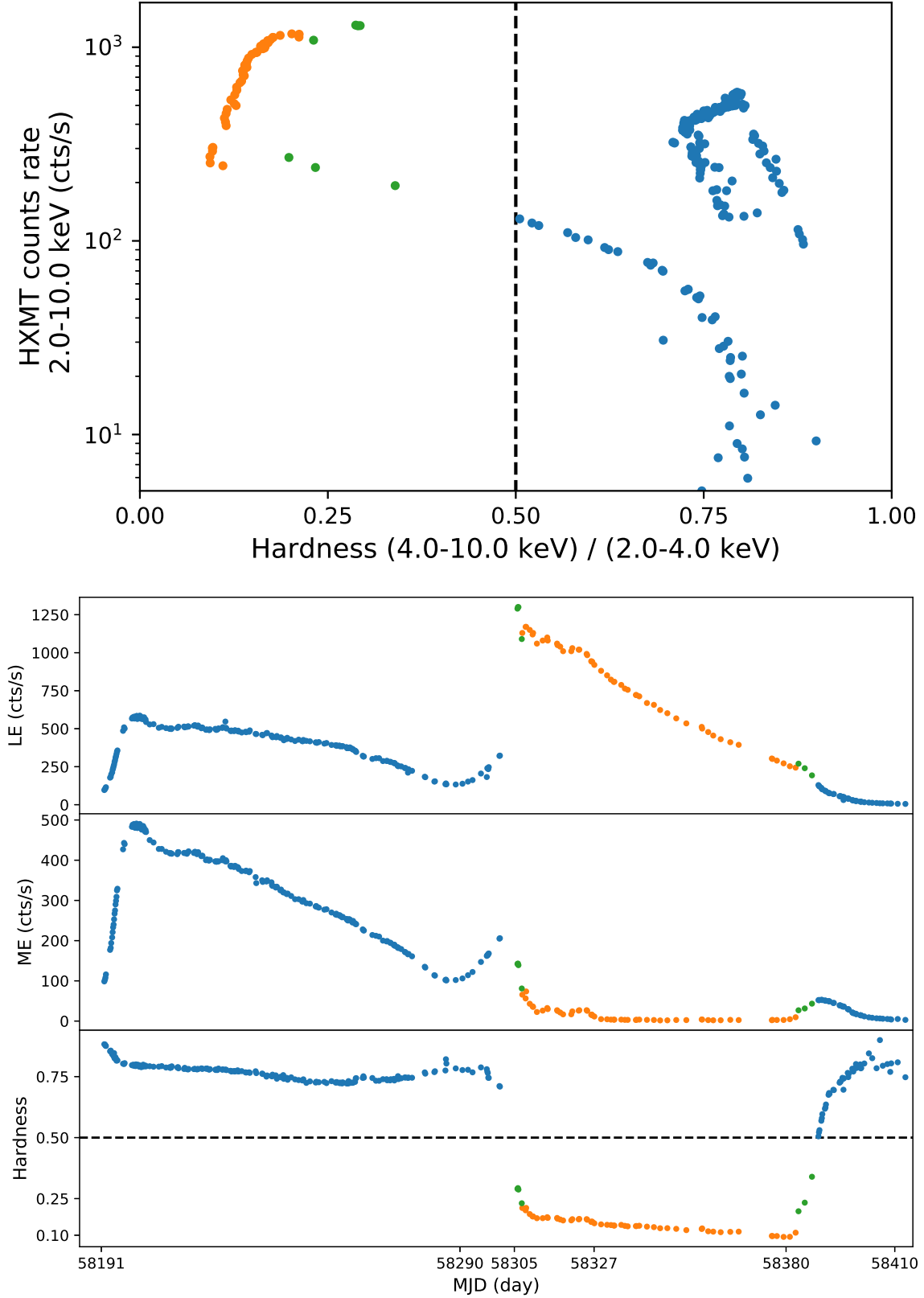


**Figure 1.** *Insight*-HXMT observations of MAXI J1820+070 covering its entire outburst. From top to bottom: the hardness-intensity diagram (HID), LE lightcurve, ME lightcurve, the evolution of the hardness ratio. The black dashed lines indicate the hardness ratio is 0.5. The blue points represent that the source is in the low/hard state, which are not analyzed in this paper. The orange and green symbols indicate observations with smaller and larger  $f_{sc}$ , respectively.

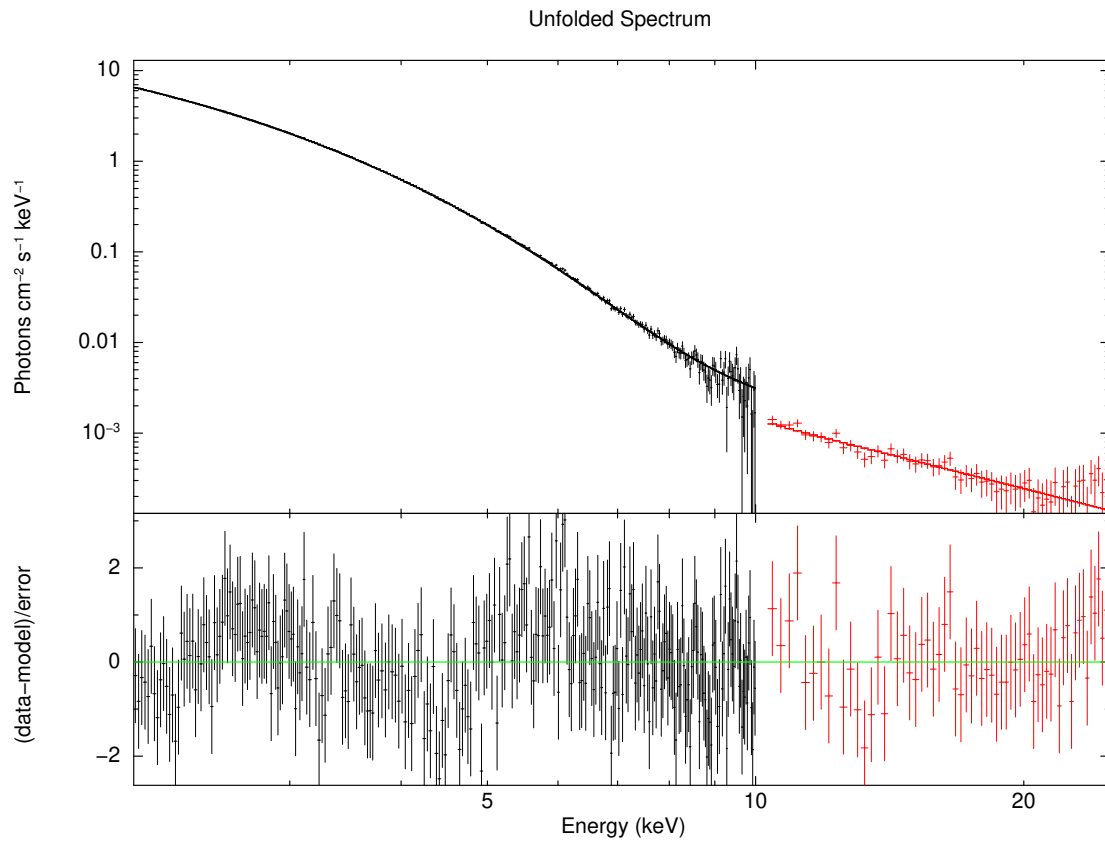


**Figure 2.** A representative (ObsID P011466110701) unfolded spectrum. The spectrum was rebinned just for the purpose of display.

**Table 1.** *Insight*-HXMT Observational Journal of MAXI J1820+070<sup>a</sup>

Number	ObsID	MJD	Start Time	End Time	exposure(s)	State <sup>b</sup>
1	P011466108401	58305.86277	2018-07-06T20:41:17	2018-07-06T23:48:23	1674 & 2155	IM
2	P011466108402	58305.99270	2018-07-06T23:48:23	2018-07-07T03:12:37	1374 & 2556	IM
3	P011466108403	58306.13453	2018-07-07T03:12:37	2018-07-07T06:22:11	810 & 1658	IM/HSS
4	P011466108501	58307.05589	2018-07-08T01:19:23	2018-07-08T04:43:34	1211 & 2014	IM/HSS
5	P011466108502	58307.19769	2018-07-08T04:43:34	2018-07-08T09:24:42	695 & 1534	IM/HSS
6	P011466108601	58308.11641	2018-07-09T02:46:32	2018-07-09T06:14:59	747 & 1114	IM/HSS
7	P011466108602	58308.26117	2018-07-09T06:14:59	2018-07-09T10:51:44	539 & 1799	IM/HSS
8	P011466108702	58309.25513	2018-07-10T06:06:17	2018-07-10T09:07:54	479 & 1423	IM/HSS
9	P011466108801	58310.03858	2018-07-11T00:54:27	2018-07-11T04:17:01	1556 & 1343	IM/HSS
10	P011466108802	58310.17925	2018-07-11T04:17:01	2018-07-11T07:24:09	898 & 941	IM/HSS
11	P011466108901	58311.23160	2018-07-12T05:32:24	2018-07-12T10:29:02	931 & 2358	HSS
12	P011466109001	58312.82233	2018-07-13T19:43:03	2018-07-14T00:44:39	2134 & 2934	HSS
13	P011466109101	58314.08167	2018-07-15T01:56:30	2018-07-15T05:23:05	1002 & 1027	HSS
14	P011466109102	58314.22513	2018-07-15T05:23:05	2018-07-15T09:07:27	1195 & 1968	HSS
15	P011466109201	58316.79946	2018-07-17T19:10:07	2018-07-17T22:15:11	1077 & 1903	HSS
16	P011466109202	58316.92798	2018-07-17T22:15:11	2018-07-18T01:39:17	1305 & 1272	HSS
17	P011466109301	58317.66130	2018-07-18T15:51:10	2018-07-18T20:44:08	1077 & 3420	HSS
18	P011466109401	58318.45692	2018-07-19T10:56:52	2018-07-19T15:52:51	1257 & 3160	HSS
19	P011466109501	58320.71167	2018-07-21T17:03:42	2018-07-21T20:59:14	3039 & 2818	HSS
20	P011466109503	58321.00778	2018-07-22T00:10:06	2018-07-22T02:50:58	479 & 760	HSS
21	P011466109601	58322.76842	2018-07-23T18:25:25	2018-07-23T22:17:50	2298 & 2554	HSS
22	P011466109602	58322.92982	2018-07-23T22:17:50	2018-07-24T02:28:17	1270 & 1777	HSS
23	P011466109701	58324.95915	2018-07-25T23:00:04	2018-07-26T02:47:29	1564 & 2244	HSS
24	P011466109702	58325.11707	2018-07-26T02:47:29	2018-07-26T05:27:31	1583 & 1776	HSS
25	P011466109801	58326.22091	2018-07-27T05:17:00	2018-07-27T09:01:17	2454 & 2360	HSS
26	P011466109802	58326.37666	2018-07-27T09:01:17	2018-07-27T12:12:12	2453 & 2228	HSS
27	P011466109803	58326.50924	2018-07-27T12:12:12	2018-07-27T14:55:38	2213 & 1981	HSS
28	P011466109901	58327.08413	2018-07-28T02:00:03	2018-07-28T06:50:58	2544 & 3874	HSS
29	P011466110001	58328.94229	2018-07-29T22:35:48	2018-07-30T03:26:25	2523 & 4027	HSS
30	P011466110101	58330.60005	2018-07-31T14:22:58	2018-07-31T19:13:23	2261 & 4219	HSS
31	P011466110201	58331.66060	2018-08-01T15:50:10	2018-08-01T20:40:32	3700 & 3544	HSS
32	P011466110301	58332.45593	2018-08-02T10:55:26	2018-08-02T14:35:40	2101 & 4263	HSS
33	P011466110302	58332.60887	2018-08-02T14:35:40	2018-08-02T18:56:37	2573 & 3701	HSS
34	P011466110401	58334.51027	2018-08-04T12:13:41	2018-08-04T15:55:25	2829 & 4762	HSS
35	P011466110701	58335.50424	2018-08-05T12:05:00	2018-08-05T16:55:15	4219 & 5276	HSS
36	P011466110801	58336.29941	2018-08-06T07:10:03	2018-08-06T12:00:50	1841 & 3871	HSS
37	P011466110901	58338.55235	2018-08-08T13:14:17	2018-08-08T16:58:34	3286 & 4320	HSS
38	P011466110902	58338.70810	2018-08-08T16:58:34	2018-08-08T19:40:25	1137 & 1704	HSS
39	P011466111001	58339.48006	2018-08-09T11:30:11	2018-08-09T16:20:53	3044 & 4386	HSS
40	P011466111201	58341.60057	2018-08-11T14:23:43	2018-08-11T19:20:41	2514 & 3491	HSS
41	P011466111301	58343.52242	2018-08-13T12:31:11	2018-08-13T17:21:47	2155 & 3185	HSS
42	P011466111401	58345.24557	2018-08-15T05:52:31	2018-08-15T10:43:08	2692 & 3519	HSS
43	P011466111501	58347.23405	2018-08-17T05:35:56	2018-08-17T10:26:31	2514 & 3516	HSS
44	P011466111601	58349.68682	2018-08-19T16:27:55	2018-08-19T21:18:31	1735 & 2693	HSS
45	P011466111701	58352.47157	2018-08-22T11:17:57	2018-08-22T16:08:32	1648 & 2758	HSS
46	P011466111801	58356.71551	2018-08-26T17:09:14	2018-08-26T20:09:34	599 & 700	HSS
47	P011466111802	58356.84074	2018-08-26T20:09:34	2018-08-27T01:15:46	180 & 658	HSS
48	P011466111901	58358.50582	2018-08-28T12:07:17	2018-08-28T16:57:46	1542 & 3007	HSS
49	P011466112001	58359.89813	2018-08-29T21:32:12	2018-08-30T02:23:11	1317 & 1938	HSS
50	P011466112101	58361.95323	2018-08-31T22:51:33	2018-09-01T03:42:27	1594 & 3417	HSS
51	P011466112201	58364.60463	2018-09-03T14:29:34	2018-09-03T19:20:11	958 & 1976	HSS
52	P011466112301	58366.92445	2018-09-05T22:10:06	2018-09-06T01:27:46	406 & 2095	HSS
53	P011466112401	58376.07197	2018-09-15T01:42:32	2018-09-15T05:26:46	1834 & 2182	HSS
54	P011466112402	58376.22769	2018-09-15T05:26:46	2018-09-15T08:08:25	539 & 941	HSS
55	P011466112501	58377.46444	2018-09-16T11:07:41	2018-09-16T15:58:08	3111 & 2702	HSS
56	P011466112601	58379.32135	2018-09-18T07:41:38	2018-09-18T12:35:16	2655 & 2825	HSS
57	P011466112701	58381.04584	2018-09-20T01:04:54	2018-09-20T05:55:25	2076 & 2251	IM
58	P011466112801	58382.63775	2018-09-21T15:17:15	2018-09-21T20:10:31	1900 & 1990	IM
59	P011466112901	58383.43367	2018-09-22T10:23:23	2018-09-22T15:16:09	3638 & 3029	IM
60	P011466113001	58385.15798	2018-09-24T03:46:23	2018-09-24T08:36:49	2910 & 2894	IM
61	P011466113101	58387.14719	2018-09-26T03:30:51	2018-09-26T08:21:12	3694 & 3042	IM

NOTE—<sup>a</sup>The log of *Insight*-HXMT observations analyzed in this work. In columns 2–7, we show the following information, respectively: observation ID; MJD; the start time of the observations; the end time of the observations; the effective exposure times in units of second for LE and ME; accretion states.

<sup>b</sup>We adopted the states defined in [Shidatsu et al. \(2019\)](#). "IM" and "HSS" represent the intermediate and high/soft state, respectively. It is noted that [Buisson et al. \(2019\)](#) classified spectra 3-10 as HSS.

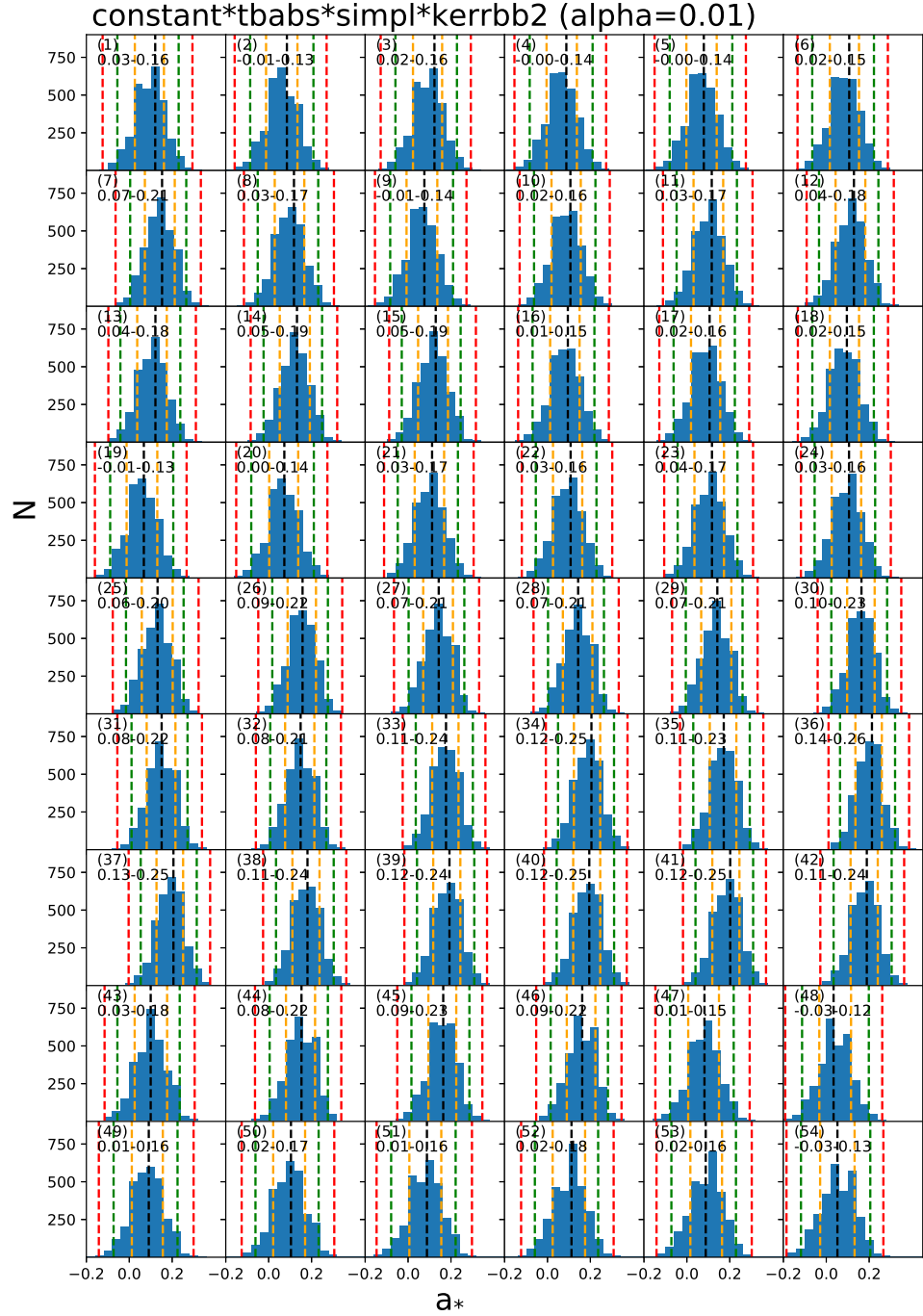


**Figure 3.** Histograms of  $a_*$  calculated via the Monte Carlo analysis for 3000 sets of parameters per spectrum. The three dashed lines imply the 99.7% ( $3\sigma$ , red), 95.4% ( $2\sigma$ , green), and 68.3% ( $1\sigma$ , orange) error, respectively. The respective 68.3% confidence level on  $a_*$  is indicated in each panel.

**Table 2.** Best-fit parameters for spectra with the model CONSTANT\*TBABS\*SIMPL\*DISKBB

Number	ObsID	SIMPL		DISKBB		CONSTANT	Reduced $\chi^2_\nu$	$\chi^2/\text{d.o.f.}$
		$\Gamma$	$f_{\text{sc}}$	$T_{\text{in}}$	$R_{\text{in}}$	norm		
1	P011466108502	2.18 ± 0.02	0.061 ± 0.001	0.738 ± 0.002	4.56 ± 0.50	0.76 ± 0.01	1.38	1505.4 / 1090
2	P011466108601	2.24 ± 0.02	0.054 ± 0.001	0.740 ± 0.002	4.65 ± 0.49	0.77 ± 0.01	1.31	1414.1 / 1079
3	P011466108602	2.16 ± 0.02	0.058 ± 0.001	0.743 ± 0.002	4.55 ± 0.51	0.85 ± 0.01	1.28	1344.6 / 1053
4	P011466108702	2.12 ± 0.02	0.035 ± 0.001	0.742 ± 0.002	4.64 ± 0.51	0.75 ± 0.02	1.20	1197.1 / 997
5	P011466108801	2.15 ± 0.03	0.030 ± 0.001	0.741 ± 0.001	4.66 ± 0.41	0.77 ± 0.01	1.36	1539.6 / 1135
6	P011466108802	2.07 ± 0.03	0.026 ± 0.001	0.743 ± 0.001	4.62 ± 0.45	0.76 ± 0.02	1.30	1371.5 / 1059
7	P011466108901	2.01 ± 0.03	0.018 ± 0.001	0.749 ± 0.001	4.45 ± 0.42	0.71 ± 0.02	1.15	1184.4 / 1034
8	P011466109001	2.03 ± 0.02	0.020 ± 0.001	0.745 ± 0.001	4.54 ± 0.37	0.71 ± 0.01	1.50	1724.3 / 1148
9	P011466109101	2.21 ± 0.03	0.029 ± 0.001	0.736 ± 0.001	4.68 ± 0.45	0.78 ± 0.02	1.19	1268.7 / 1070
10	P011466109102	2.04 ± 0.03	0.022 ± 0.001	0.741 ± 0.001	4.60 ± 0.42	0.74 ± 0.01	1.31	1411.1 / 1080
11	P011466109201	1.99 ± 0.03	0.021 ± 0.001	0.740 ± 0.001	4.56 ± 0.42	0.68 ± 0.01	1.20	1270.8 / 1060
12	P011466109202	2.16 ± 0.04	0.022 ± 0.001	0.741 ± 0.001	4.54 ± 0.41	0.77 ± 0.02	1.30	1396.8 / 1076
13	P011466109301	2.02 ± 0.03	0.017 ± 0.001	0.740 ± 0.001	4.54 ± 0.41	0.70 ± 0.02	1.28	1336.3 / 1041
14	P011466109401	2.00 ± 0.03	0.015 ± 0.001	0.739 ± 0.001	4.50 ± 0.40	0.65 ± 0.02	1.24	1301.2 / 1050
15	P011466109501	2.19 ± 0.03	0.017 ± 0.001	0.738 ± 0.001	4.51 ± 0.35	0.71 ± 0.01	1.44	1694.1 / 1177
16	P011466109503	2.18 ± 0.05	0.022 ± 0.001	0.732 ± 0.002	4.64 ± 0.52	0.76 ± 0.03	1.06	996.0 / 942
17	P011466109601	2.10 ± 0.03	0.022 ± 0.001	0.732 ± 0.001	4.60 ± 0.38	0.75 ± 0.01	1.38	1610.7 / 1168
18	P011466109602	2.07 ± 0.03	0.022 ± 0.001	0.730 ± 0.001	4.62 ± 0.42	0.73 ± 0.02	1.34	1451.2 / 1084
19	P011466109701	2.07 ± 0.03	0.024 ± 0.001	0.722 ± 0.001	4.69 ± 0.42	0.69 ± 0.01	1.22	1377.0 / 1126
20	P011466109702	2.08 ± 0.03	0.023 ± 0.001	0.723 ± 0.001	4.68 ± 0.42	0.69 ± 0.01	1.26	1418.5 / 1122
21	P011466109801	2.20 ± 0.04	0.017 ± 0.001	0.725 ± 0.001	4.58 ± 0.38	0.70 ± 0.02	1.29	1507.0 / 1164
22	P011466109802	2.25 ± 0.04	0.019 ± 0.001	0.722 ± 0.001	4.60 ± 0.38	0.71 ± 0.02	1.42	1630.3 / 1151
23	P011466109803	2.32 ± 0.05	0.019 ± 0.001	0.723 ± 0.001	4.59 ± 0.39	0.70 ± 0.02	1.31	1487.6 / 1138
24	P011466109901	2.23 ± 0.04	0.015 ± 0.001	0.721 ± 0.001	4.60 ± 0.37	0.64 ± 0.02	1.20	1398.9 / 1161
25	P011466110001	3.25 ± 0.09	0.026 ± 0.002	0.715 ± 0.001	4.60 ± 0.42	0.63 ± 0.03	1.17	1293.0 / 1104
26	P011466110101	3.05 ± 0.10	0.019 ± 0.002	0.717 ± 0.001	4.50 ± 0.41	0.64 ± 0.03	1.19	1293.5 / 1089
27	P011466110201	4.50 ± 0.15	0.070 ± 0.008	0.695 ± 0.002	4.74 ± 0.53	0.78 ± 0.04	1.06	1257.3 / 1186
28	P011466110301	3.51 ± 0.13	0.031 ± 0.004	0.703 ± 0.002	4.61 ± 0.47	0.57 ± 0.03	1.07	1151.8 / 1072
29	P011466110302	4.41 ± 0.16	0.063 ± 0.007	0.694 ± 0.002	4.74 ± 0.53	0.78 ± 0.04	1.14	1252.5 / 1099
30	P011466110401	4.17 ± 0.12	0.064 ± 0.006	0.694 ± 0.002	4.67 ± 0.51	0.68 ± 0.03	1.10	1241.0 / 1131
31	P011466110701	4.38 ± 0.14	0.069 ± 0.007	0.687 ± 0.002	4.72 ± 0.52	0.65 ± 0.03	1.02	1220.8 / 1191
32	P011466110801	4.37 ± 0.18	0.065 ± 0.009	0.685 ± 0.002	4.74 ± 0.58	0.65 ± 0.04	1.10	1156.8 / 1049
33	P011466110901	4.50 ± 0.15	0.078 ± 0.009	0.681 ± 0.002	4.68 ± 0.56	0.68 ± 0.04	1.06	1183.5 / 1117
34	P011466110902	4.50 ± 0.22	0.075 ± 0.012	0.683 ± 0.003	4.64 ± 0.65	0.80 ± 0.06	0.92	885.2 / 962
35	P011466111001	4.07 ± 0.12	0.068 ± 0.006	0.679 ± 0.002	4.68 ± 0.53	0.64 ± 0.03	0.95	1069.1 / 1124
36	P011466111201	4.50 ± 0.14	0.090 ± 0.010	0.672 ± 0.003	4.65 ± 0.58	0.78 ± 0.04	1.09	1158.5 / 1063
37	P011466111301	4.50 ± 0.18	0.078 ± 0.011	0.672 ± 0.003	4.63 ± 0.60	0.73 ± 0.05	0.97	1010.9 / 1041
38	P011466111401	4.50 ± 0.14	0.102 ± 0.011	0.656 ± 0.003	4.79 ± 0.64	0.63 ± 0.04	1.78	1901.8 / 1069
39	P011466111501	4.50 ± 0.14	0.110 ± 0.012	0.650 ± 0.003	4.81 ± 0.66	0.61 ± 0.04	1.51	1601.5 / 1061
40	P011466111601	4.50 ± 0.16	0.099 ± 0.012	0.644 ± 0.003	4.80 ± 0.69	0.78 ± 0.05	1.12	1109.0 / 993
41	P011466111701	4.50 ± 0.20	0.075 ± 0.012	0.644 ± 0.003	4.72 ± 0.66	0.86 ± 0.07	0.98	978.6 / 995
42	P011466111801	3.66 ± 0.23	0.055 ± 0.011	0.641 ± 0.004	4.68 ± 0.78	0.69 ± 0.08	0.98	835.0 / 854
43	P011466111802	2.26 ± 0.23	0.022 ± 0.005	0.642 ± 0.005	4.66 ± 0.87	0.24 ± 0.04	0.86	614.7 / 712
44	P011466111901	3.76 ± 0.17	0.051 ± 0.007	0.630 ± 0.003	4.77 ± 0.65	0.60 ± 0.05	0.90	883.0 / 986
45	P011466112001	4.43 ± 0.24	0.089 ± 0.017	0.616 ± 0.004	4.91 ± 0.82	0.66 ± 0.07	0.97	918.1 / 951
46	P011466112101	4.50 ± 0.18	0.100 ± 0.014	0.606 ± 0.004	4.99 ± 0.79	0.83 ± 0.07	0.91	893.7 / 978
47	P011466112201	2.90 ± 0.14	0.034 ± 0.005	0.609 ± 0.003	4.89 ± 0.72	0.40 ± 0.03	0.95	862.7 / 905
48	P011466112301	2.48 ± 0.17	0.025 ± 0.004	0.604 ± 0.003	4.92 ± 0.83	0.26 ± 0.03	0.86	678.7 / 785
49	P011466112401	3.86 ± 0.17	0.064 ± 0.010	0.565 ± 0.003	5.20 ± 0.84	0.72 ± 0.07	0.93	896.6 / 961
50	P011466112402	2.77 ± 0.23	0.022 ± 0.005	0.581 ± 0.003	4.86 ± 0.84	0.55 ± 0.08	0.85	643.2 / 757
51	P011466112501	2.74 ± 0.11	0.024 ± 0.003	0.576 ± 0.002	4.90 ± 0.61	0.49 ± 0.04	0.92	959.4 / 1047
52	P011466112601	3.31 ± 0.13	0.038 ± 0.005	0.564 ± 0.002	5.00 ± 0.68	0.78 ± 0.06	1.00	1005.5 / 1009
53	P011466112701	2.65 ± 0.09	0.024 ± 0.002	0.558 ± 0.002	5.01 ± 0.66	0.80 ± 0.05	1.04	1019.5 / 976
54	P011466112801	2.27 ± 0.06	0.027 ± 0.002	0.548 ± 0.002	5.09 ± 0.68	0.83 ± 0.03	1.01	1022.9 / 1011
55	P011466108401	2.34 ± 0.01	0.158 ± 0.002	0.741 ± 0.002	4.46 ± 0.48	0.82 ± 0.01	2.02	2411.2 / 1194
56	P011466108402	2.27 ± 0.01	0.152 ± 0.002	0.745 ± 0.002	4.41 ± 0.48	0.78 ± 0.01	1.86	2224.5 / 1194
57	P011466108403	2.30 ± 0.01	0.153 ± 0.002	0.733 ± 0.002	4.60 ± 0.55	0.77 ± 0.01	1.41	1657.2 / 1178
58	P011466108501	2.21 ± 0.01	0.086 ± 0.001	0.725 ± 0.002	4.59 ± 0.48	0.75 ± 0.01	1.58	1868.5 / 1180
59	P011466112901	2.23 ± 0.02	0.082 ± 0.002	0.546 ± 0.002	4.88 ± 0.65	0.80 ± 0.01	1.18	1414.6 / 1194
60	P011466113001	2.17 ± 0.02	0.100 ± 0.002	0.534 ± 0.002	4.71 ± 0.70	0.82 ± 0.01	1.10	1317.0 / 1192
61	P011466113101	2.12 ± 0.01	0.167 ± 0.002	0.488 ± 0.003	4.75 ± 0.88	0.88 ± 0.01	1.08	1294.3 / 1194

NOTE—In column 3-9, we show the following information: the dimensionless photon index of power-law  $\Gamma$ ; the scattered fraction  $f_{\text{sc}}$ ; the temperature of inner disk radius  $T_{\text{in}}$  in the unit of keV; the inner radius  $R_{\text{in}}$  of the thin accretion disk in the unit of gravitational radius; the normalization constant; the reduced chi-square; the total chi-square  $\chi^2$  and degrees of freedom d.o.f..

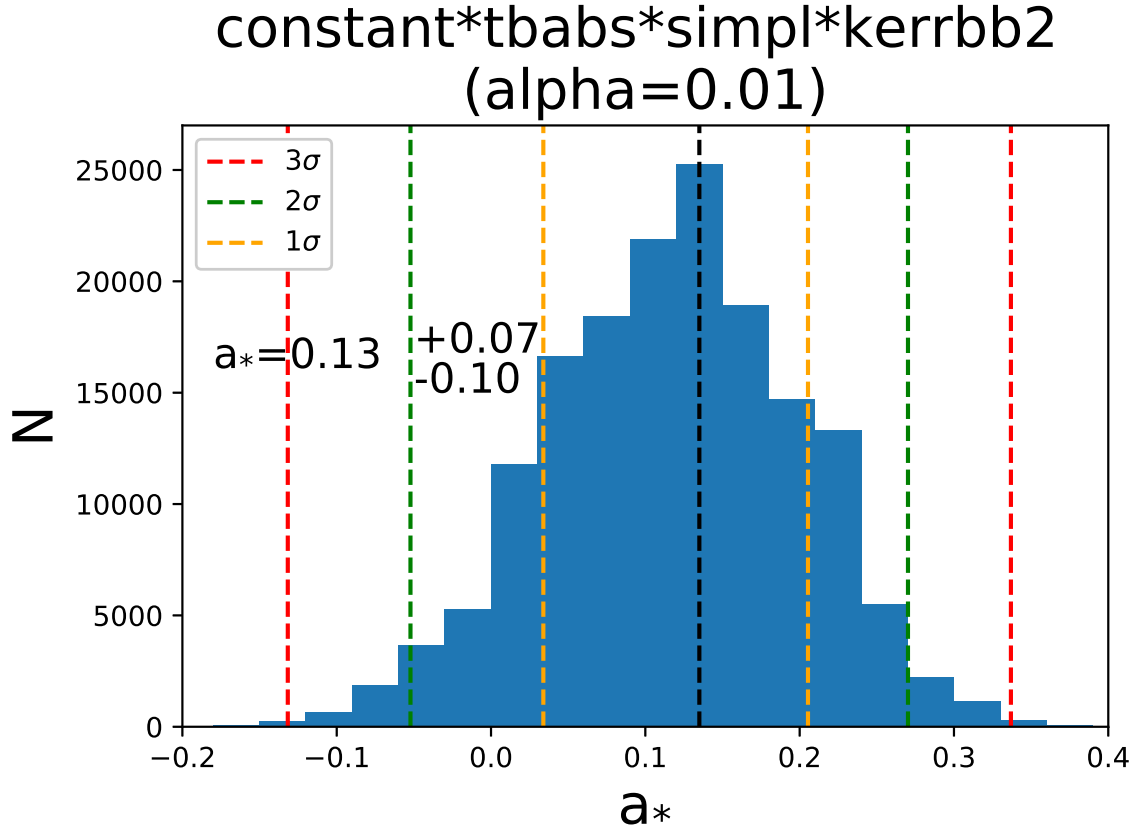


**Figure 4.** Summed histogram of  $a_*$  for 54 spectra, including 162000 data points.

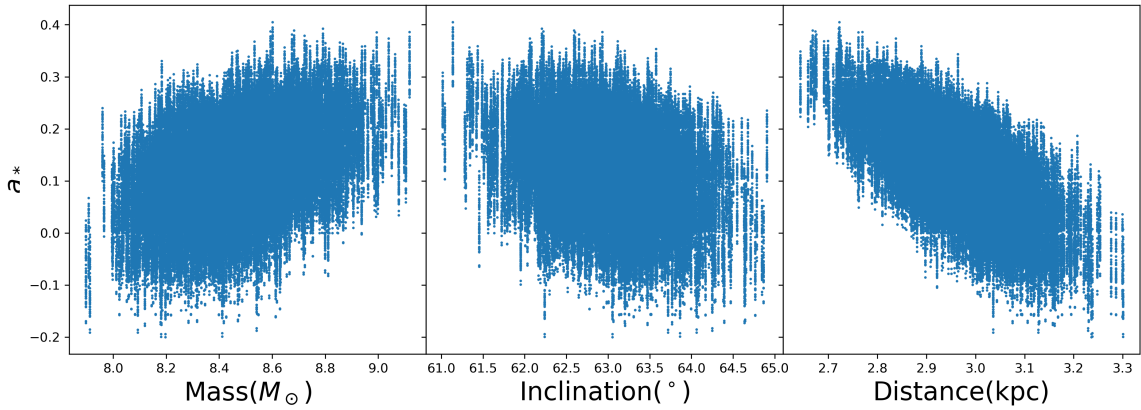


**Figure 5.** Correlation plots for our MC simulations, displaying the effect on the spin of varying  $M$ ,  $i$  and  $D$ . Each panel contains 162000 data points (see Figure 4).

**Table 3.** Best-fit parameters for spectra with the model CONSTANT\*TBABS\*SIMPL\*KERRBB2 ( $\alpha = 0.01$ )

Number	ObsID	SIMPL		KERRBB2		CONSTANT	Reduced $\chi^2_\nu$	$\chi^2/\text{d.o.f.}$
		$\Gamma$	$f_{sc}$	$a_*^a$	$\dot{M}^b$	norm		
1	P011466108502	2.15 ± 0.02	0.097 ± 0.002	0.121 ± 0.009	2.74 ± 0.03	0.85 ± 0.01	1.17	1278.3 / 1090
2	P011466108601	2.20 ± 0.02	0.085 ± 0.002	0.085 ± 0.011	2.94 ± 0.03	0.87 ± 0.02	1.10	1190.3 / 1079
3	P011466108602	2.15 ± 0.02	0.094 ± 0.002	0.123 ± 0.010	2.79 ± 0.03	0.97 ± 0.02	1.11	1165.9 / 1053
4	P011466108702	2.11 ± 0.02	0.056 ± 0.002	0.088 ± 0.012	2.93 ± 0.03	0.88 ± 0.02	1.05	1051.2 / 997
5	P011466108801	2.07 ± 0.03	0.044 ± 0.001	0.079 ± 0.008	2.93 ± 0.02	0.88 ± 0.02	1.04	1178.5 / 1135
6	P011466108802	1.98 ± 0.03	0.037 ± 0.001	0.107 ± 0.007	2.85 ± 0.02	0.88 ± 0.03	1.01	1073.7 / 1059
7	P011466108901	1.99 ± 0.03	0.025 ± 0.001	0.153 ± 0.007	2.63 ± 0.02	0.90 ± 0.03	0.94	968.8 / 1034
8	P011466109001	1.97 ± 0.02	0.029 ± 0.001	0.118 ± 0.005	2.77 ± 0.01	0.85 ± 0.02	1.09	1256.9 / 1148
9	P011466109101	2.12 ± 0.03	0.041 ± 0.002	0.076 ± 0.009	2.89 ± 0.02	0.91 ± 0.03	0.94	1001.0 / 1070
10	P011466109102	1.99 ± 0.03	0.033 ± 0.001	0.107 ± 0.006	2.79 ± 0.02	0.88 ± 0.02	1.01	1094.5 / 1080
11	P011466109201	1.95 ± 0.03	0.031 ± 0.001	0.116 ± 0.006	2.72 ± 0.02	0.81 ± 0.02	0.97	1026.6 / 1060
12	P011466109202	2.04 ± 0.04	0.029 ± 0.001	0.129 ± 0.006	2.68 ± 0.02	0.93 ± 0.03	0.98	1057.3 / 1076
13	P011466109301	2.00 ± 0.03	0.024 ± 0.001	0.122 ± 0.006	2.68 ± 0.02	0.90 ± 0.03	1.01	1048.4 / 1041
14	P011466109401	1.97 ± 0.03	0.020 ± 0.001	0.132 ± 0.006	2.61 ± 0.02	0.84 ± 0.03	1.00	1044.8 / 1050
15	P011466109501	2.06 ± 0.03	0.022 ± 0.001	0.129 ± 0.004	2.61 ± 0.01	0.88 ± 0.02	0.97	1146.8 / 1177
16	P011466109503	2.12 ± 0.05	0.032 ± 0.002	0.095 ± 0.013	2.73 ± 0.03	0.93 ± 0.04	0.93	878.8 / 942
17	P011466109601	2.01 ± 0.03	0.031 ± 0.001	0.106 ± 0.005	2.67 ± 0.01	0.87 ± 0.02	0.98	1141.6 / 1168
18	P011466109602	2.01 ± 0.03	0.033 ± 0.001	0.096 ± 0.009	2.69 ± 0.02	0.85 ± 0.02	1.05	1136.9 / 1084
19	P011466109701	2.01 ± 0.03	0.036 ± 0.001	0.068 ± 0.007	2.71 ± 0.02	0.79 ± 0.02	0.97	1095.0 / 1126
20	P011466109702	2.00 ± 0.03	0.034 ± 0.001	0.073 ± 0.007	2.69 ± 0.02	0.79 ± 0.02	0.99	1114.0 / 1122
21	P011466109801	2.05 ± 0.04	0.022 ± 0.001	0.112 ± 0.005	2.53 ± 0.01	0.86 ± 0.03	0.94	1089.7 / 1164
22	P011466109802	2.08 ± 0.04	0.024 ± 0.001	0.108 ± 0.005	2.53 ± 0.01	0.85 ± 0.03	1.04	1192.3 / 1151
23	P011466109803	2.09 ± 0.05	0.022 ± 0.001	0.117 ± 0.005	2.51 ± 0.01	0.84 ± 0.03	0.97	1103.3 / 1138
24	P011466109901	2.10 ± 0.04	0.018 ± 0.001	0.106 ± 0.004	2.51 ± 0.01	0.84 ± 0.03	0.91	1059.3 / 1161
25	P011466110001	2.50(f)	0.015 ± 0.001	0.132 ± 0.005	2.38 ± 0.01	0.86 ± 0.04	0.90	994.0 / 1105
26	P011466110101	2.50(f)	0.011 ± 0.001	0.158 ± 0.006	2.26 ± 0.01	1.06 ± 0.06	0.91	992.9 / 1090
27	P011466110201	2.50(f)	0.014 ± 0.000	0.143 ± 0.005	2.25 ± 0.01	0.73 ± 0.03	0.89	1053.2 / 1187
28	P011466110301	2.50(f)	0.014 ± 0.001	0.143 ± 0.006	2.22 ± 0.01	0.73 ± 0.04	0.91	979.8 / 1073
29	P011466110302	2.50(f)	0.013 ± 0.001	0.142 ± 0.005	2.22 ± 0.01	0.80 ± 0.04	0.96	1059.3 / 1100
30	P011466110401	2.50(f)	0.018 ± 0.001	0.164 ± 0.006	2.13 ± 0.01	0.61 ± 0.02	0.98	1113.8 / 1132
31	P011466110701	2.50(f)	0.016 ± 0.001	0.151 ± 0.005	2.12 ± 0.01	0.57 ± 0.02	0.85	1010.0 / 1192
32	P011466110801	2.50(f)	0.014 ± 0.001	0.149 ± 0.006	2.10 ± 0.01	0.63 ± 0.03	0.97	1021.6 / 1050
33	P011466110901	2.50(f)	0.017 ± 0.001	0.177 ± 0.006	1.97 ± 0.01	0.54 ± 0.02	0.96	1071.9 / 1118
34	P011466110902	2.50(f)	0.015 ± 0.001	0.205 ± 0.005	1.91 ± 0.01	0.72 ± 0.05	0.87	840.6 / 963
35	P011466111001	2.50(f)	0.023 ± 0.001	0.172 ± 0.006	1.96 ± 0.01	0.53 ± 0.02	0.85	951.5 / 1125
36	P011466111201	2.50(f)	0.018 ± 0.001	0.213 ± 0.004	1.80 ± 0.01	0.60 ± 0.03	0.94	995.6 / 1064
37	P011466111301	2.50(f)	0.017 ± 0.001	0.206 ± 0.004	1.79 ± 0.01	0.57 ± 0.03	0.92	959.8 / 1042
38	P011466111401	2.50(f)	0.016 ± 0.001	0.181 ± 0.007	1.78 ± 0.01	0.39 ± 0.02	0.93	992.5 / 1070
39	P011466111501	2.50(f)	0.020 ± 0.001	0.193 ± 0.008	1.71 ± 0.01	0.38 ± 0.02	0.95	1011.7 / 1062
40	P011466111601	2.50(f)	0.020 ± 0.001	0.195 ± 0.009	1.64 ± 0.02	0.52 ± 0.02	0.92	914.8 / 994
41	P011466111701	2.50(f)	0.016 ± 0.001	0.202 ± 0.005	1.58 ± 0.01	0.63 ± 0.04	0.97	968.8 / 996
42	P011466111801	2.50(f)	0.027 ± 0.001	0.189 ± 0.015	1.54 ± 0.02	0.57 ± 0.04	0.95	811.1 / 855
43	P011466111802	2.50(f)	0.045 ± 0.002	0.100 ± 0.032	1.66 ± 0.05	0.33 ± 0.03	0.88	626.5 / 713
44	P011466111901	2.50(f)	0.023 ± 0.001	0.153 ± 0.008	1.53 ± 0.01	0.46 ± 0.02	0.90	890.2 / 987
45	P011466112001	2.50(f)	0.023 ± 0.001	0.164 ± 0.010	1.47 ± 0.02	0.39 ± 0.03	0.98	928.7 / 952
46	P011466112101	2.50(f)	0.023 ± 0.001	0.162 ± 0.009	1.42 ± 0.01	0.45 ± 0.02	0.92	895.9 / 979
47	P011466112201	2.50(f)	0.037 ± 0.001	0.082 ± 0.014	1.50 ± 0.02	0.39 ± 0.02	0.96	866.9 / 906
48	P011466112301	2.50(f)	0.042 ± 0.002	0.034 ± 0.018	1.52 ± 0.03	0.31 ± 0.02	0.89	699.7 / 786
49	P011466112401	2.50(f)	0.028 ± 0.001	0.091 ± 0.014	1.24 ± 0.02	0.44 ± 0.02	0.94	907.3 / 962
50	P011466112402	2.50(f)	0.027 ± 0.001	0.104 ± 0.013	1.21 ± 0.02	0.57 ± 0.04	0.84	634.3 / 758
51	P011466112501	2.50(f)	0.030 ± 0.001	0.088 ± 0.011	1.20 ± 0.01	0.50 ± 0.02	0.92	967.2 / 1048
52	P011466112601	2.50(f)	0.027 ± 0.001	0.112 ± 0.007	1.13 ± 0.01	0.60 ± 0.02	0.98	993.4 / 1010
53	P011466112701	2.27 ± 0.09	0.026 ± 0.003	0.088 ± 0.018	1.11 ± 0.02	0.73 ± 0.05	1.02	994.4 / 976
54	P011466112801	2.10 ± 0.06	0.038 ± 0.002	0.052 ± 0.016	1.10 ± 0.02	0.80 ± 0.04	0.98	995.3 / 1011
55	P011466108401	2.30 ± 0.01	0.244 ± 0.003	0.136 ± 0.009	2.82 ± 0.02	0.89 ± 0.01	1.64	1959.9 / 1194
56	P011466108402	2.24 ± 0.01	0.238 ± 0.002	0.146 ± 0.010	2.80 ± 0.03	0.85 ± 0.01	1.52	1814.1 / 1194
57	P011466108403	2.28 ± 0.01	0.242 ± 0.003	0.071 ± 0.014	3.02 ± 0.04	0.84 ± 0.01	1.23	1449.0 / 1178
58	P011466108501	2.17 ± 0.01	0.136 ± 0.002	0.115 ± 0.008	2.65 ± 0.02	0.81 ± 0.01	1.30	1530.3 / 1180
59	P011466112901	2.16 ± 0.02	0.130 ± 0.003	0.124 ± 0.012	0.98 ± 0.01	0.80 ± 0.01	1.14	1361.0 / 1194
60	P011466113001	2.13 ± 0.02	0.161 ± 0.003	0.179 ± 0.018	0.82 ± 0.02	0.82 ± 0.01	1.06	1258.6 / 1192
61	P011466113101	2.09 ± 0.01	0.262 ± 0.003	0.221 ± 0.019	0.59 ± 0.01	0.89 ± 0.01	1.06	1263.6 / 1194

NOTE—<sup>a</sup> the dimensionless spin parameter  $a_*$ .<sup>b</sup> the mass accretion rate  $\dot{M}$  in units of  $10^{18} \text{ g s}^{-1}$ .

**Table 4.** Best-fit parameters for spectra with the model CONSTANT\*TBABS\*SIMPL\*KERRBB2 ( $\alpha = 0.1$ )

Number	ObsID	SIMPL		KERRBB2		CONSTANT	Reduced $\chi^2_\nu$	$\chi^2/\text{d.o.f.}$
		$\Gamma$	$f_{\text{sc}}$	$a_*^a$	$\dot{M}^b$			
1	P011466108502	2.16 ± 0.02	0.098 ± 0.002	0.052 ± 0.011	2.87 ± 0.03	0.86 ± 0.01	1.17	1279.0 / 1090
2	P011466108601	2.19 ± 0.02	0.083 ± 0.002	0.028 ± 0.009	3.04 ± 0.03	0.87 ± 0.02	1.10	1189.7 / 1079
3	P011466108602	2.15 ± 0.02	0.095 ± 0.002	0.054 ± 0.012	2.92 ± 0.03	0.97 ± 0.02	1.11	1167.2 / 1053
4	P011466108702	2.11 ± 0.02	0.055 ± 0.002	0.028 ± 0.010	3.03 ± 0.03	0.89 ± 0.02	1.05	1050.7 / 997
5	P011466108801	2.06 ± 0.03	0.043 ± 0.001	0.021 ± 0.006	3.03 ± 0.02	0.88 ± 0.02	1.04	1179.0 / 1135
6	P011466108802	1.99 ± 0.03	0.038 ± 0.001	0.037 ± 0.008	2.98 ± 0.02	0.88 ± 0.03	1.01	1071.6 / 1059
7	P011466108901	2.00 ± 0.03	0.026 ± 0.001	0.095 ± 0.009	2.74 ± 0.02	0.90 ± 0.03	0.94	972.8 / 1034
8	P011466109001	1.98 ± 0.02	0.029 ± 0.001	0.052 ± 0.006	2.89 ± 0.02	0.85 ± 0.02	1.09	1256.8 / 1148
9	P011466109101	2.12 ± 0.04	0.041 ± 0.002	0.018 ± 0.007	2.99 ± 0.02	0.92 ± 0.03	0.94	1002.4 / 1070
10	P011466109102	2.00 ± 0.03	0.033 ± 0.001	0.038 ± 0.007	2.91 ± 0.02	0.88 ± 0.02	1.01	1093.5 / 1080
11	P011466109201	1.96 ± 0.03	0.031 ± 0.001	0.050 ± 0.007	2.84 ± 0.02	0.81 ± 0.02	0.97	1026.6 / 1060
12	P011466109202	2.05 ± 0.04	0.030 ± 0.001	0.064 ± 0.007	2.79 ± 0.02	0.93 ± 0.03	0.98	1058.6 / 1076
13	P011466109301	2.01 ± 0.03	0.025 ± 0.001	0.057 ± 0.007	2.80 ± 0.02	0.89 ± 0.03	1.01	1050.5 / 1041
14	P011466109401	1.98 ± 0.03	0.021 ± 0.001	0.070 ± 0.007	2.72 ± 0.02	0.84 ± 0.03	1.00	1047.8 / 1050
15	P011466109501	2.07 ± 0.03	0.023 ± 0.001	0.066 ± 0.006	2.72 ± 0.01	0.88 ± 0.02	0.98	1149.2 / 1177
16	P011466109503	2.11 ± 0.05	0.031 ± 0.002	0.033 ± 0.010	2.84 ± 0.03	0.94 ± 0.04	0.93	878.2 / 942
17	P011466109601	2.01 ± 0.03	0.031 ± 0.001	0.038 ± 0.006	2.79 ± 0.02	0.87 ± 0.02	0.97	1138.4 / 1168
18	P011466109602	2.00 ± 0.03	0.032 ± 0.001	0.036 ± 0.007	2.78 ± 0.02	0.86 ± 0.02	1.05	1134.1 / 1084
19	P011466109701	2.00 ± 0.03	0.036 ± 0.001	0.012 ± 0.006	2.80 ± 0.02	0.79 ± 0.02	0.97	1097.1 / 1126
20	P011466109702	2.00 ± 0.03	0.033 ± 0.001	0.017 ± 0.006	2.78 ± 0.02	0.80 ± 0.02	0.99	1115.5 / 1122
21	P011466109801	2.06 ± 0.04	0.022 ± 0.001	0.047 ± 0.006	2.64 ± 0.01	0.86 ± 0.03	0.93	1088.1 / 1164
22	P011466109802	2.09 ± 0.04	0.024 ± 0.001	0.042 ± 0.006	2.65 ± 0.01	0.85 ± 0.03	1.03	1189.4 / 1151
23	P011466109803	2.10 ± 0.05	0.022 ± 0.001	0.052 ± 0.006	2.62 ± 0.02	0.84 ± 0.03	0.97	1102.6 / 1138
24	P011466109901	2.11 ± 0.04	0.018 ± 0.001	0.041 ± 0.005	2.62 ± 0.01	0.84 ± 0.03	0.91	1057.5 / 1161
25	P011466110001	2.50(f)	0.015 ± 0.001	0.074 ± 0.006	2.47 ± 0.01	0.85 ± 0.03	0.90	996.9 / 1105
26	P011466110101	2.50(f)	0.011 ± 0.001	0.108 ± 0.004	2.34 ± 0.01	1.07 ± 0.06	0.91	996.6 / 1090
27	P011466110201	2.50(f)	0.015 ± 0.001	0.089 ± 0.006	2.33 ± 0.01	0.72 ± 0.03	0.89	1056.8 / 1187
28	P011466110301	2.50(f)	0.014 ± 0.001	0.091 ± 0.007	2.30 ± 0.02	0.72 ± 0.04	0.91	981.8 / 1073
29	P011466110302	2.50(f)	0.013 ± 0.001	0.088 ± 0.006	2.31 ± 0.01	0.78 ± 0.04	0.97	1063.2 / 1100
30	P011466110401	2.50(f)	0.018 ± 0.001	0.113 ± 0.004	2.20 ± 0.01	0.62 ± 0.02	0.99	1116.7 / 1132
31	P011466110701	2.50(f)	0.017 ± 0.001	0.103 ± 0.004	2.19 ± 0.01	0.57 ± 0.02	0.85	1013.8 / 1192
32	P011466110801	2.50(f)	0.015 ± 0.001	0.102 ± 0.005	2.17 ± 0.01	0.63 ± 0.04	0.98	1024.9 / 1050
33	P011466110901	2.50(f)	0.017 ± 0.001	0.125 ± 0.004	2.04 ± 0.01	0.55 ± 0.02	0.96	1071.8 / 1118
34	P011466110902	2.50(f)	0.015 ± 0.001	0.144 ± 0.007	2.00 ± 0.02	0.73 ± 0.05	0.87	839.4 / 963
35	P011466111001	2.50(f)	0.023 ± 0.001	0.120 ± 0.004	2.03 ± 0.01	0.54 ± 0.02	0.85	951.8 / 1125
36	P011466111201	2.50(f)	0.018 ± 0.001	0.155 ± 0.005	1.87 ± 0.01	0.61 ± 0.03	0.93	994.5 / 1064
37	P011466111301	2.50(f)	0.017 ± 0.001	0.146 ± 0.006	1.87 ± 0.01	0.58 ± 0.03	0.92	957.5 / 1042
38	P011466111401	2.50(f)	0.016 ± 0.001	0.128 ± 0.005	1.84 ± 0.01	0.40 ± 0.02	0.93	991.5 / 1070
39	P011466111501	2.50(f)	0.019 ± 0.001	0.138 ± 0.005	1.77 ± 0.01	0.40 ± 0.02	0.95	1008.2 / 1062
40	P011466111601	2.50(f)	0.019 ± 0.001	0.141 ± 0.007	1.70 ± 0.01	0.54 ± 0.03	0.92	911.8 / 994
41	P011466111701	2.50(f)	0.016 ± 0.001	0.142 ± 0.007	1.65 ± 0.01	0.64 ± 0.04	0.97	967.4 / 996
42	P011466111801	2.50(f)	0.027 ± 0.001	0.135 ± 0.011	1.60 ± 0.02	0.59 ± 0.04	0.95	810.5 / 855
43	P011466111802	2.50(f)	0.044 ± 0.002	0.044 ± 0.024	1.72 ± 0.04	0.34 ± 0.03	0.88	626.9 / 713
44	P011466111901	2.50(f)	0.023 ± 0.001	0.107 ± 0.006	1.58 ± 0.01	0.47 ± 0.02	0.90	890.0 / 987
45	P011466112001	2.50(f)	0.023 ± 0.001	0.116 ± 0.007	1.52 ± 0.01	0.40 ± 0.03	0.98	928.7 / 952
46	P011466112101	2.50(f)	0.023 ± 0.001	0.116 ± 0.007	1.47 ± 0.01	0.46 ± 0.02	0.92	896.8 / 979
47	P011466112201	2.50(f)	0.037 ± 0.001	0.025 ± 0.011	1.55 ± 0.02	0.40 ± 0.02	0.96	867.0 / 906
48	P011466112301	2.50(f)	0.042 ± 0.001	-0.007 ± 0.022	1.55 ± 0.03	0.32 ± 0.02	0.89	699.0 / 786
49	P011466112401	2.50(f)	0.028 ± 0.001	0.035 ± 0.010	1.28 ± 0.01	0.46 ± 0.03	0.94	906.5 / 962
50	P011466112402	2.50(f)	0.027 ± 0.001	0.045 ± 0.018	1.26 ± 0.02	0.59 ± 0.04	0.84	634.3 / 758
51	P011466112501	2.50(f)	0.030 ± 0.001	0.026 ± 0.008	1.25 ± 0.01	0.52 ± 0.02	0.92	967.5 / 1048
52	P011466112601	2.50(f)	0.027 ± 0.001	0.052 ± 0.009	1.18 ± 0.01	0.63 ± 0.03	0.98	993.0 / 1010
53	P011466112701	2.25 ± 0.10	0.026 ± 0.003	0.029 ± 0.012	1.15 ± 0.01	0.74 ± 0.06	1.02	993.5 / 976
54	P011466112801	2.09 ± 0.06	0.038 ± 0.002	0.002 ± 0.012	1.13 ± 0.01	0.81 ± 0.04	0.98	995.6 / 1011
55	P011466108401	2.30 ± 0.01	0.246 ± 0.003	0.064 ± 0.011	2.97 ± 0.03	0.90 ± 0.01	1.65	1964.7 / 1194
56	P011466108402	2.25 ± 0.01	0.240 ± 0.002	0.076 ± 0.011	2.95 ± 0.03	0.85 ± 0.01	1.53	1821.1 / 1194
57	P011466108403	2.27 ± 0.01	0.241 ± 0.003	0.019 ± 0.012	3.11 ± 0.03	0.84 ± 0.01	1.23	1451.2 / 1178
58	P011466108501	2.17 ± 0.01	0.137 ± 0.002	0.044 ± 0.009	2.78 ± 0.02	0.81 ± 0.01	1.30	1529.2 / 1180
59	P011466112901	2.17 ± 0.02	0.131 ± 0.003	0.056 ± 0.015	1.03 ± 0.02	0.81 ± 0.01	1.14	1360.6 / 1194
60	P011466113001	2.12 ± 0.02	0.160 ± 0.003	0.126 ± 0.014	0.85 ± 0.01	0.82 ± 0.01	1.06	1257.7 / 1192
61	P011466113101	2.10 ± 0.01	0.262 ± 0.003	0.145 ± 0.024	0.62 ± 0.02	0.89 ± 0.01	1.06	1263.2 / 1194

**Table 5.** Best-fit parameters for spectra with the model CONSTANT\*TBABS\*SIMPL\*KERRBB2 ( $M = 8.06 M_{\odot}$ ,  $i = 66.2^{\circ}$ )

Number	ObsID	SIMPL		KERRBB2		CONSTANT	Reduced $\chi^2_{\nu}$	$\chi^2/\text{d.o.f.}$
		$\Gamma$	$f_{\text{sc}}$	$a_*$ <sup>a</sup>	$\dot{M}$ <sup>b</sup>	norm		
1	P011466108502	2.16 ± 0.02	0.099 ± 0.002	-0.136 ± 0.013	3.65 ± 0.04	0.85 ± 0.01	1.18	1285.4 / 1090
2	P011466108601	2.19 ± 0.02	0.085 ± 0.002	-0.163 ± 0.011	3.86 ± 0.03	0.87 ± 0.02	1.11	1194.4 / 1079
3	P011466108602	2.15 ± 0.02	0.096 ± 0.002	-0.133 ± 0.014	3.71 ± 0.04	0.96 ± 0.02	1.11	1172.5 / 1053
4	P011466108702	2.11 ± 0.02	0.056 ± 0.002	-0.161 ± 0.012	3.85 ± 0.04	0.88 ± 0.02	1.06	1053.5 / 997
5	P011466108801	2.06 ± 0.03	0.044 ± 0.001	-0.170 ± 0.007	3.85 ± 0.02	0.88 ± 0.02	1.04	1184.5 / 1135
6	P011466108802	1.99 ± 0.03	0.039 ± 0.001	-0.151 ± 0.009	3.78 ± 0.03	0.88 ± 0.03	1.02	1077.7 / 1059
7	P011466108901	2.00 ± 0.03	0.026 ± 0.001	-0.082 ± 0.007	3.46 ± 0.02	0.90 ± 0.03	0.94	973.5 / 1034
8	P011466109001	1.98 ± 0.02	0.030 ± 0.001	-0.133 ± 0.007	3.66 ± 0.02	0.84 ± 0.02	1.10	1264.7 / 1148
9	P011466109101	2.12 ± 0.04	0.042 ± 0.002	-0.173 ± 0.009	3.79 ± 0.03	0.91 ± 0.03	0.94	1007.0 / 1070
10	P011466109102	2.00 ± 0.03	0.034 ± 0.001	-0.150 ± 0.008	3.69 ± 0.03	0.88 ± 0.02	1.02	1099.8 / 1080
11	P011466109201	1.96 ± 0.03	0.032 ± 0.001	-0.136 ± 0.009	3.60 ± 0.03	0.81 ± 0.02	0.97	1030.2 / 1060
12	P011466109202	2.06 ± 0.04	0.031 ± 0.001	-0.119 ± 0.009	3.54 ± 0.03	0.92 ± 0.03	0.99	1065.2 / 1076
13	P011466109301	2.01 ± 0.03	0.025 ± 0.001	-0.128 ± 0.009	3.55 ± 0.03	0.89 ± 0.03	1.02	1056.7 / 1041
14	P011466109401	1.99 ± 0.03	0.021 ± 0.001	-0.111 ± 0.009	3.44 ± 0.02	0.83 ± 0.03	1.00	1051.7 / 1050
15	P011466109501	2.08 ± 0.03	0.023 ± 0.001	-0.116 ± 0.007	3.44 ± 0.02	0.88 ± 0.02	0.98	1158.1 / 1177
16	P011466109503	2.12 ± 0.05	0.032 ± 0.002	-0.156 ± 0.012	3.60 ± 0.04	0.94 ± 0.04	0.93	879.9 / 942
17	P011466109601	2.02 ± 0.03	0.032 ± 0.001	-0.151 ± 0.007	3.54 ± 0.02	0.87 ± 0.02	0.98	1146.2 / 1168
18	P011466109602	2.01 ± 0.03	0.033 ± 0.001	-0.153 ± 0.008	3.53 ± 0.02	0.86 ± 0.02	1.05	1139.7 / 1084
19	P011466109701	2.01 ± 0.03	0.036 ± 0.001	-0.181 ± 0.007	3.56 ± 0.02	0.79 ± 0.02	0.98	1100.0 / 1126
20	P011466109702	2.00 ± 0.03	0.034 ± 0.001	-0.176 ± 0.007	3.53 ± 0.02	0.79 ± 0.02	1.00	1119.4 / 1122
21	P011466109801	2.07 ± 0.04	0.023 ± 0.001	-0.141 ± 0.007	3.35 ± 0.02	0.86 ± 0.03	0.94	1093.8 / 1164
22	P011466109802	2.10 ± 0.04	0.025 ± 0.001	-0.147 ± 0.007	3.36 ± 0.02	0.85 ± 0.03	1.04	1195.5 / 1151
23	P011466109803	2.11 ± 0.05	0.023 ± 0.001	-0.134 ± 0.007	3.32 ± 0.02	0.84 ± 0.03	0.97	1108.1 / 1138
24	P011466109901	2.11 ± 0.04	0.018 ± 0.001	-0.147 ± 0.007	3.32 ± 0.02	0.84 ± 0.03	0.91	1059.6 / 1161
25	P011466110001	2.50(f)	0.016 ± 0.001	-0.109 ± 0.007	3.13 ± 0.02	0.83 ± 0.03	0.91	1000.7 / 1105
26	P011466110101	2.50(f)	0.012 ± 0.001	-0.076 ± 0.006	2.97 ± 0.02	1.05 ± 0.06	0.91	996.5 / 1090
27	P011466110201	2.50(f)	0.015 ± 0.001	-0.091 ± 0.005	2.95 ± 0.01	0.72 ± 0.03	0.89	1057.5 / 1187
28	P011466110301	2.50(f)	0.014 ± 0.001	-0.091 ± 0.006	2.91 ± 0.02	0.71 ± 0.04	0.91	980.7 / 1073
29	P011466110302	2.50(f)	0.013 ± 0.001	-0.091 ± 0.005	2.91 ± 0.01	0.79 ± 0.04	0.97	1064.4 / 1100
30	P011466110401	2.50(f)	0.019 ± 0.001	-0.069 ± 0.006	2.80 ± 0.01	0.61 ± 0.02	0.99	1115.9 / 1132
31	P011466110701	2.50(f)	0.017 ± 0.001	-0.082 ± 0.005	2.78 ± 0.01	0.56 ± 0.02	0.85	1012.7 / 1192
32	P011466110801	2.50(f)	0.015 ± 0.001	-0.084 ± 0.006	2.75 ± 0.02	0.62 ± 0.04	0.98	1024.0 / 1050
33	P011466110901	2.50(f)	0.017 ± 0.001	-0.055 ± 0.006	2.59 ± 0.01	0.54 ± 0.02	0.96	1073.7 / 1118
34	P011466110902	2.50(f)	0.016 ± 0.001	-0.030 ± 0.009	2.53 ± 0.02	0.70 ± 0.05	0.87	840.1 / 963
35	P011466111001	2.50(f)	0.023 ± 0.001	-0.061 ± 0.006	2.58 ± 0.01	0.53 ± 0.02	0.85	951.2 / 1125
36	P011466111201	2.50(f)	0.018 ± 0.001	-0.016 ± 0.007	2.37 ± 0.02	0.59 ± 0.02	0.94	997.5 / 1064
37	P011466111301	2.50(f)	0.017 ± 0.001	-0.029 ± 0.008	2.37 ± 0.02	0.56 ± 0.03	0.92	960.3 / 1042
38	P011466111401	2.50(f)	0.017 ± 0.001	-0.054 ± 0.006	2.34 ± 0.01	0.39 ± 0.02	0.93	991.4 / 1070
39	P011466111501	2.50(f)	0.020 ± 0.001	-0.043 ± 0.007	2.26 ± 0.02	0.39 ± 0.02	0.95	1009.8 / 1062
40	P011466111601	2.50(f)	0.020 ± 0.001	-0.042 ± 0.008	2.17 ± 0.02	0.53 ± 0.03	0.92	913.9 / 994
41	P011466111701	2.50(f)	0.016 ± 0.001	-0.042 ± 0.009	2.10 ± 0.02	0.63 ± 0.04	0.97	966.9 / 996
42	P011466111801	2.50(f)	0.027 ± 0.001	-0.053 ± 0.014	2.04 ± 0.03	0.58 ± 0.04	0.95	810.3 / 855
43	P011466111802	2.50(f)	0.045 ± 0.002	-0.162 ± 0.027	2.20 ± 0.05	0.34 ± 0.03	0.88	626.1 / 713
44	P011466111901	2.50(f)	0.023 ± 0.001	-0.089 ± 0.008	2.02 ± 0.02	0.47 ± 0.02	0.90	888.2 / 987
45	P011466112001	2.50(f)	0.023 ± 0.001	-0.078 ± 0.009	1.94 ± 0.02	0.39 ± 0.03	0.97	927.6 / 952
46	P011466112101	2.50(f)	0.023 ± 0.001	-0.078 ± 0.009	1.87 ± 0.02	0.46 ± 0.02	0.92	896.8 / 979
47	P011466112201	2.50(f)	0.038 ± 0.001	-0.185 ± 0.012	1.98 ± 0.02	0.40 ± 0.02	0.96	865.5 / 906
48	P011466112301	2.50(f)	0.042 ± 0.001	-0.234 ± 0.026	2.00 ± 0.04	0.32 ± 0.02	0.89	698.3 / 786
49	P011466112401	2.50(f)	0.028 ± 0.001	-0.171 ± 0.011	1.63 ± 0.02	0.45 ± 0.03	0.94	906.0 / 962
50	P011466112402	2.50(f)	0.027 ± 0.001	-0.160 ± 0.020	1.60 ± 0.03	0.58 ± 0.04	0.84	634.0 / 758
51	P011466112501	2.50(f)	0.031 ± 0.001	-0.182 ± 0.009	1.60 ± 0.01	0.51 ± 0.02	0.92	964.6 / 1048
52	P011466112601	2.50(f)	0.027 ± 0.001	-0.154 ± 0.011	1.50 ± 0.01	0.61 ± 0.02	0.98	992.1 / 1010
53	P011466112701	2.25 ± 0.10	0.026 ± 0.003	-0.182 ± 0.014	1.47 ± 0.02	0.73 ± 0.05	1.02	993.1 / 976
54	P011466112801	2.10 ± 0.06	0.039 ± 0.002	-0.231 ± 0.021	1.47 ± 0.02	0.80 ± 0.04	0.98	994.9 / 1011
55	P011466108401	2.31 ± 0.01	0.248 ± 0.003	-0.125 ± 0.012	3.78 ± 0.04	0.90 ± 0.01	1.66	1981.0 / 1194
56	P011466108402	2.24 ± 0.01	0.238 ± 0.002	-0.086 ± 0.010	3.68 ± 0.03	0.85 ± 0.01	1.54	1835.2 / 1194
57	P011466108403	2.27 ± 0.01	0.242 ± 0.003	-0.176 ± 0.014	3.96 ± 0.04	0.84 ± 0.01	1.24	1457.5 / 1178
58	P011466108501	2.18 ± 0.01	0.138 ± 0.002	-0.147 ± 0.011	3.53 ± 0.03	0.81 ± 0.01	1.30	1538.8 / 1180
59	P011466112901	2.17 ± 0.02	0.132 ± 0.003	-0.153 ± 0.019	1.31 ± 0.02	0.80 ± 0.01	1.14	1361.0 / 1194
60	P011466113001	2.13 ± 0.02	0.162 ± 0.003	-0.058 ± 0.021	1.08 ± 0.02	0.82 ± 0.01	1.06	1258.4 / 1192
61	P011466113101	2.10 ± 0.01	0.264 ± 0.003	-0.035 ± 0.037	0.79 ± 0.03	0.88 ± 0.01	1.06	1263.9 / 1194

**Table 6.** Effect of Different  $\Gamma$  (only for P011466110701)<sup>a</sup>

N	Model	Parameter	Case 1	Case 2	Case 3	Case 4
1	SIMPL	$\Gamma$	2.00(f)	2.30(f)	2.50(f)	2.80(f)
2	SIMPL	$f_{sc}$	$0.010 \pm 0.001$	$0.013 \pm 0.001$	$0.017 \pm 0.001$	$0.022 \pm 0.001$
3	KERRBB2	$a_*$	$0.165 \pm 0.005$	$0.157 \pm 0.005$	$0.151 \pm 0.005$	$0.141 \pm 0.005$
4	KERRBB2	$\dot{M}$	$2.09 \pm 0.01$	$2.11 \pm 0.01$	$2.12 \pm 0.01$	$2.14 \pm 0.01$
5	CONSTANT	norm	$0.42 \pm 0.02$	$0.51 \pm 0.02$	$0.57 \pm 0.02$	$0.67 \pm 0.02$
6		Reduced $\chi^2_\nu$	0.89	0.86	0.85	0.83
7		$\chi^2/\text{d.o.f.}$	1063.2/1192	1026.2/1192	1010.0/1192	997.19/1192

- Mitsuda, K., Inoue, H., Koyama, K., et al. 1984, PASJ, 36, 741
- Morningstar, W. R., Miller, J. M., Reis, R. C., & Ebisawa, K. 2014, ApJL, 784, L18, doi: [10.1088/2041-8205/784/2/L18](https://doi.org/10.1088/2041-8205/784/2/L18)
- Noble, S. C., Krolik, J. H., & Hawley, J. F. 2009, ApJ, 692, 411, doi: [10.1088/0004-637X/692/1/411](https://doi.org/10.1088/0004-637X/692/1/411)
- . 2010, ApJ, 711, 959, doi: [10.1088/0004-637X/711/2/959](https://doi.org/10.1088/0004-637X/711/2/959)
- Noble, S. C., Krolik, J. H., Schnittman, J. D., & Hawley, J. F. 2011, ApJ, 743, 115, doi: [10.1088/0004-637X/743/2/115](https://doi.org/10.1088/0004-637X/743/2/115)
- Novikov, I. D., & Thorne, K. S. 1973, in Black Holes (Les Astres Occlus), 343–450
- Penna, R. F., McKinney, J. C., Narayan, R., et al. 2010, MNRAS, 408, 752, doi: [10.1111/j.1365-2966.2010.17170.x](https://doi.org/10.1111/j.1365-2966.2010.17170.x)
- Remillard, R. A., & McClintock, J. E. 2006, ARA&A, 44, 49, doi: [10.1146/annurev.astro.44.051905.092532](https://doi.org/10.1146/annurev.astro.44.051905.092532)
- Reynolds, C. S., & Fabian, A. C. 2008, ApJ, 675, 1048, doi: [10.1086/527344](https://doi.org/10.1086/527344)
- Reynolds, C. S., & Nowak, M. A. 2003, PhR, 377, 389, doi: [10.1016/S0370-1573\(02\)00584-7](https://doi.org/10.1016/S0370-1573(02)00584-7)
- Shafee, R., Narayan, R., & McClintock, J. E. 2008, ApJ, 676, 549, doi: [10.1086/527346](https://doi.org/10.1086/527346)
- Shappee, B. J., Prieto, J. L., Grupe, D., et al. 2014, ApJ, 788, 48, doi: [10.1088/0004-637X/788/1/48](https://doi.org/10.1088/0004-637X/788/1/48)
- Shidatsu, M., Nakahira, S., Murata, K. L., et al. 2019, ApJ, 874, 183, doi: [10.3847/1538-4357/ab09ff](https://doi.org/10.3847/1538-4357/ab09ff)
- Steiner, J. F., McClintock, J. E., Orosz, J. A., et al. 2014, ApJ, 793, L29, doi: [10.1088/2041-8205/793/2/L29](https://doi.org/10.1088/2041-8205/793/2/L29)
- Steiner, J. F., McClintock, J. E., & Reid, M. J. 2012, ApJL, 745, L7, doi: [10.1088/2041-8205/745/1/L7](https://doi.org/10.1088/2041-8205/745/1/L7)
- Steiner, J. F., McClintock, J. E., Remillard, R. A., Narayan, R., & Gou, L. 2009a, ApJL, 701, L83, doi: [10.1088/0004-637X/701/2/L83](https://doi.org/10.1088/0004-637X/701/2/L83)
- Steiner, J. F., Narayan, R., McClintock, J. E., & Ebisawa, K. 2009b, PASP, 121, 1279, doi: [10.1086/648535](https://doi.org/10.1086/648535)
- Steiner, J. F., Walton, D. J., García, J. A., et al. 2016, ApJ, 817, 154, doi: [10.3847/0004-637X/817/2/154](https://doi.org/10.3847/0004-637X/817/2/154)
- Steiner, J. F., Reis, R. C., McClintock, J. E., et al. 2011, MNRAS, 416, 941, doi: [10.1111/j.1365-2966.2011.19089.x](https://doi.org/10.1111/j.1365-2966.2011.19089.x)
- Torres, M. A. P., Casares, J., Jiménez-Ibarra, F., et al. 2020, ApJL, 893, L37, doi: [10.3847/2041-8213/ab863a](https://doi.org/10.3847/2041-8213/ab863a)
- . 2019, ApJL, 882, L21, doi: [10.3847/2041-8213/ab39df](https://doi.org/10.3847/2041-8213/ab39df)
- Tripathi, A., Zhou, M., Abdikamalov, A. B., et al. 2020, ApJ, 897, 84, doi: [10.3847/1538-4357/ab9600](https://doi.org/10.3847/1538-4357/ab9600)
- Tucker, M. A., Shappee, B. J., Holoiien, T. W. S., et al. 2018, ApJL, 867, L9, doi: [10.3847/2041-8213/aae88a](https://doi.org/10.3847/2041-8213/aae88a)
- Uttley, P., Gendreau, K., Markwardt, C., et al. 2018, The Astronomer’s Telegram, 11423, 1
- Wong, T.-W., Valsecchi, F., Fragos, T., & Kalogera, V. 2012, ApJ, 747, 111, doi: [10.1088/0004-637X/747/2/111](https://doi.org/10.1088/0004-637X/747/2/111)
- Zhang, S. N., Cui, W., & Chen, W. 1997, ApJ, 482, L155, doi: [10.1086/310705](https://doi.org/10.1086/310705)
- Zhang, S. N., Li, T. P., Lu, F. J., et al. 2020, Sci. China-Phys. Mech. Astron, 63(4): 249502, doi: [10.1007/s11433-019-1432-6](https://doi.org/10.1007/s11433-019-1432-6)